Annu. Rev. Mater. Sci. 1993. 23:321–79

INORGANIC CRYSTALS FOR NONLINEAR OPTICAL FREQUENCY CONVERSION

Peter F. Bordui

Crystal Technology, Inc., 1040 E. Meadow Circle, Palo Alto, California 94303

Martin M. Fejer

Department of Applied Physics, Stanford University, Stanford, California 94305

KEY WORDS: lasers, nonlinear optics, second harmonic generation, crystal growth, materials processing

INTRODUCTION

Although the well-known properties of laser radiation are desirable for a wide variety of applications, only limited segments of the optical spectrum can be directly produced by practical, high-performance laser systems. Through nonlinear optics, laser radiation can be converted from one frequency to another, significantly increasing the range of applications that can be addressed.

In a general nonlinear optical (NLO) interaction, one or two laser beams are directed into a suitable material in which an output beam of the desired frequency is generated. NLO interactions include harmonic generation, sum and difference frequency generation, and parametric oscillation, the latter generating a pair of tunable output beams at lower frequency from a single input beam.

The physics of an NLO interaction impose severe demands on potential NLO materials. In general, a material must be optically transparent to the incident and generated radiation, possess a quadratic susceptibility of

0084–6600/93/0801–0321$02.00

sufficient magnitude, allow for phasematching of the interaction, and withstand the laser intensity without damaging.

Since its first demonstration in 1961 (1), nonlinear frequency conversion has been a materials-limited field, with practical advances largely controlled by progress in making available improved NLO materials. To date, the most important class of materials used in nonlinear optics has been inorganic single crystals. Single crystals are particularly well-suited to the physics of the NLO process. Organic materials, although promising, have yet to be produced with sufficiently robust chemical and mechanical properties to find broad practical application.

The aim of this review is to survey the processing and properties of inorganic single crystals used in NLO frequency conversion. We consider both general issues and specific families of materials. We begin by considering the NLO frequency conversion process itself and the associated implications for NLO material requirements.

FUNDAMENTALS OF NLO FREQUENCY CONVERSION

In a typical frequency conversion device, one or two waves are input to a crystal, with the goal of generating at the output of the crystal one or two waves at different desired frequencies. Such interactions involve three waves at frequencies $\omega_3 \geq \omega_2 \geq \omega_1$, which must obey $\omega_3 = \omega_2 + \omega_1$. The coupling of these waves is through the nonlinear polarization $\mathbf{P}$, which contains frequency components at the sum, difference, and second harmonic of the input frequencies. $\mathbf{P}$ is related to the electric fields $\mathbf{E}$ by the nonlinear susceptibility $\mathbf{d}$, a third rank tensor characteristic of the specific nonlinear crystal. The constitutive relation in MKS units for second harmonic generation is (2) $\mathbf{P}_{2\omega} = \varepsilon_0 \mathbf{d} \mathbf{E}_{\omega}^2$, where the subscripts indicate the frequency at which the quantity is to be evaluated. For typical nonlinear crystals used in the visible and near infrared, components of $\mathbf{d}$ are in the range 0.5 to 5 pm/V, although technologically important materials with nonlinear susceptibilities several times larger and smaller exist.

In general, the small size of the nonlinear coupling requires the use of crystals greater than 1 mm in length to achieve significant conversion efficiency. As such crystals are thousands of wavelengths long, small differences between the phase velocities of the interacting fields can cause large variations in the relative phase of the waves. The direction of the energy flow between the interacting waves depends on this relative phase, so a crucial parameter in the efficiency of a frequency conversion device is the magnitude of the velocity mismatch, $\Delta k = k_3 - k_2 - k_1$, where the

propagation constants are $k_i = \omega_i n_i/c$, the index of refraction at frequency ω_i is n_i, and c is the speed of light in vacuum. An interaction for which Δk vanishes is said to be phasematched, which happens, for example, if the refractive indices are equal at all the interacting frequencies.

In the majority of this section, we focus on the specific example of second harmonic generation (SHG) in detail, because it is prototypical of other nonlinear interactions, and is perhaps the most widely used type of nonlinear frequency conversion. Following the discussion of SHG, considerations for other interactions that differ significantly from those for SHG are briefly discussed.

SHG with Undepleted Pump

The simplest form of SHG involves a plane wave at frequency ω and intensity I_ω incident on a nonlinear crystal of length L (Figure 1, top). The quantity of interest from a device standpoint is the conversion efficiency $\eta = I_{2\omega}/I_\omega$. In the low conversion efficiency limit, where we can take the fundamental intensity to be undepleted by conversion to the second harmonic, the conversion efficiency η is given by (3)

$$\eta = \eta_0 \,\mathrm{sinc}^2(\delta), \qquad 1.$$

where the nonlinear drive $\eta_0 = C^2L^2I_\omega$, the dephasing $\delta = \Delta kL/2$, the constant $C^2 = 8\pi^2 d_{eff}^2/n_1n_2n_3c\varepsilon_0\lambda^2$, where λ is the vacuum wavelength at the fundamental frequency, ε_0 is the permittivity of vacuum, d_{eff} is the effective nonlinear coefficient, n_1, n_2, and n_3 are the refractive indices of the three waves taking part in the interaction, and $\mathrm{sinc}(x) = \sin(x)/x$. We see that for a phasematched interaction, the efficiency scales quadratically with both the length of the crystal and the nonlinear susceptibility, and linearly with the intensity of the fundamental.

The efficiency decreases rapidly for a non-phasematched interaction, decreasing to 50% of the phasematched value when $\delta = 0.443\pi$. For SHG with a 1 μm fundamental in a 1 cm long crystal, $\delta = 0.443\pi$ for $n_{2\omega} - n_\omega = 2 \times 10^{-5}$. Thus extremely close matching of the refractive indices is essential for an efficient interaction. As all media of interest are positively dispersive (typically $n_{2\omega} - n_\omega \approx 0.1$), such close matching does not occur without special steps. In the vast majority of practical devices, phasematching is accomplished through the use of anisotropic media, chosen such that the birefringence seen by orthogonally polarized waves precisely compensates for the dispersion. The requirement that such compensation be possible at the wavelength of interest often dictates the choice of nonlinear medium for a particular interaction and often limits the wavelength, temperature, and angular bandwidths of the device. To consider these points, we must briefly discuss the optics of birefringent crystals.

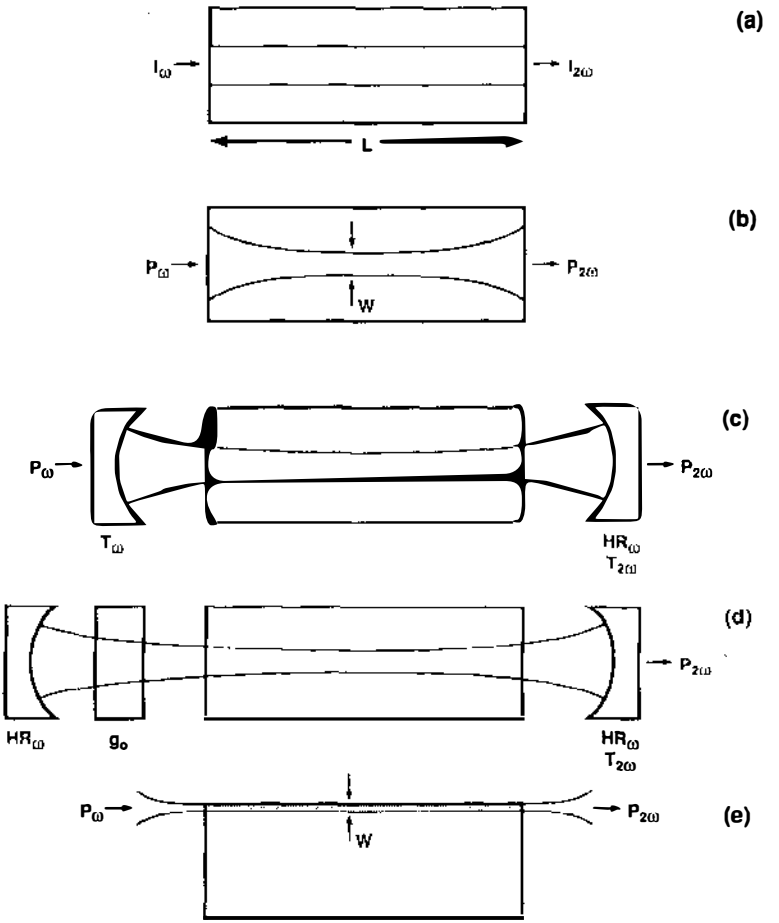

Figure 1 Configurations for second harmonic generation: (*a*) plane wave; (*b*) focused; (*c*) external resonant cavity; (*d*) intracavity; (*e*) waveguide.

Birefringent Media

Crystals with symmetries lower than cubic are birefringent, that is, the phase velocity of a wave in the crystal depends on the propagation direction and the polarization of the wave (4). Crystals with hexagonal, tetragonal, and trigonal point groups are said to be uniaxial, that is, there is a single propagation direction, known as the optical axis (that coincides with the high symmetry axis), for which the phase velocity is independent of the

polarization of the wave. For propagation at an angle θ to the optical axis, there are two nondegenerate polarization states, the ordinary wave, polarized perpendicular to the optical axis, and the extraordinary wave, polarized in the plane containing the optical axis and the propagation vector. The phase velocity of the ordinary wave is equal to c/n_o independent of θ, while the phase velocity of the extraordinary wave is $c/n_e(\theta)$, where $n_e(\theta)$ varies between n_o and n_e for $0 < \theta < \pi/2$, according to

$$n_e^{-2}(\theta) = n_e^{-2}\sin^2(\theta) + n_o^{-2}\cos^2(\theta). \qquad 2.$$

A uniaxial crystal is known as positive (negative) birefringent for $n_e > (<) n_o$.

A phenomenon contributing to an important limitation on frequency conversion devices is Poynting vector walkoff. In a birefringent medium, the direction of energy flow is separated by a small angle ρ from the phase velocity direction, which leads to a spatial separation of ordinary and extraordinary beams with parallel k-vectors. The walkoff angle, given to first order in the birefringence by $\rho \approx \bar{n}^{-1}(n_e - n_o)\sin(2\theta)$, where $\bar{n}$ is the average of n_e and n_o, is thus proportional to the birefringence, vanishes for $\theta = 0°$ and 90°, and is maximum at $\theta = 45°$.

Crystals with orthorhombic, monoclinic, and triclinic point groups are biaxial, that is, they have two optical axes. Description of wave propagation in biaxial crystals is more complex than for uniaxial crystals, but shows similar general features. An important distinction is that the phase velocity depends on two angles, θ, the angle between z and k, and ϕ, the angle between the projection of k on the x-y plane and x, with $n_x < n_y < n_z$. For θ or ϕ equal to 0 or 90°, wave propagation is similar to that in a uniaxial crystal, with one polarization having a refractive index independent of propagation direction and no walkoff, and the other having a refractive index varying as described by Equation 2 and nonzero walkoff. Reference (5) discusses a standard convention for reporting refractive indices and nonlinear coefficients.

Phasematching

The continuous variation in the extraordinary index available in birefringent crystals allows the choice of a particular propagation direction, θ_{pm}, for which $\Delta k = 0$. For a negative uniaxial crystal, this condition is achieved when the fundamental is an ordinary wave and the second harmonic is extraordinary, that is, when $n_{e,2\omega}(\theta_{pm}) = n_{o,\omega}$. For positive birefringence, e and o are reversed. If the birefringence is large enough, in addition to this Type I phasematching, it is possible to phasematch with one fundamental wave of each polarization. For negative birefringence, the condition is $n_{e,2\omega}(\theta_{pm}) = [n_{o,\omega} + n_{e,\omega}(\theta_{pm})]/2$, with the roles of e and o again

reversed for positive birefringence. This Type II phasematching can sometimes provide a more favorable phasematching angle or a larger effective nonlinearity.

The more complex case of phasematching in biaxial crystals, where both θ and ϕ must be specified, is discussed in References (5–7). In biaxial crystals, rather than a unique phasematching angle, there exist loci of allowed θ, ϕ.

Acceptance Bandwidths

An important consideration in nonlinear device design is the effect of deviations from design angle, wavelength, or temperature on the conversion efficiency. These parameters change Δk away from the ideal (zero) value achieved at phasematching, which results in a decrease in the conversion efficiency below the phasematched value. According to Equation 1, the efficiency is reduced by 50% when $|\Delta k| = 0.886\pi/L$. With Equation 2 for the angle dependence of the extraordinary index, we find the angular acceptance for Type I phasematching in a negative uniaxial crystal is, to first order in $(n_e - n_o)$,

$$|\theta - \theta_{pm}| < 0.221\lambda/L|(n_{e,2\omega} - n_{\theta,\omega})\sin(2\theta)|. \quad 3.$$

Similar relations hold for other phasematching schemes, differing only in the appropriate combination of indices of refraction. We see from Equation 3 that the angular acceptance is inversely proportional to the length and birefringence of the crystal and is smallest for $\theta = 45°$. For a typical case, with $\lambda = 1$ μm, $L = 1$ cm, $\theta = 45°$, and $n_e - n_o = 0.1$, the internal acceptance angle is $|\theta - \theta_{pm}| < 0.22$ mrad. The external acceptance angle, larger by a factor of approximately n due to refraction at the input face of the crystal, is then 0.44 mrad for $n = 2$. We see that while a large birefringence leads to broadly tunable phasematching, it also leads to an extremely tight angular tolerance that has a significant impact on device optimization for critically phasematched ($\theta_{pm} \neq 0$) interactions.

For the special case $\theta_{pm} = \pi/2$, the interaction is noncritically phasematched. For θ close to $\pi/2$, the extraordinary refractive index has no first order dependence on θ, so the expression for the angular acceptance becomes

$$|\theta - \theta_{pm}| < \sqrt{0.221\lambda/L|n_{e,2\omega} - n_{\theta,\omega}|}, \quad 4.$$

and thus depends only on the square root of the length of the crystal. For the same conditions as our previous example, the tolerance increases to $|\theta - \theta_{pm}| < 15$ mrad. The much larger angular acceptance of noncritically phasematched interactions is a significant practical advantage.

In biaxial crystals, similar considerations to these lead to two different acceptance angles, one for θ and one for ϕ. In crystals with one plane of significantly lower birefringence, these two angular acceptances can differ substantially. When the plane $\theta = \pi/2$ is of low birefringence, there are two closely spaced noncritical wavelengths (for $\phi = 0, \pi/2$), and the angular acceptance $\delta\phi$ is large over this whole range of angles, a situation of considerable practical value referred to as quasi-noncritical phasematching (8). Note that for a biaxial crystal there can be as many as six noncritical wavelengths (three Type I and three Type II), vs at most two (one Type I and one Type II) for uniaxial crystals.

Noncritical phasematching requires an alternative to angle tuning the effective birefringence for phasematching. In general, temperature tuning of the birefringence is the only viable alternative. The phasematching temperatures $T_{\rm pm}$ for Type I and Type II noncritical phasematching in negative uniaxial crystals are obtained from $n_{e,2\omega}(T_{\rm pm}) = n_{o,\omega}(T_{\rm pm})$ and $n_{e,2\omega}(T_{\rm pm}) = [n_{o,\omega}(T_{\rm pm}) + n_{e,\omega}(T_{\rm pm})]/2$, respectively. For positive uniaxial crystals, the roles of e and o are again reversed. The temperature acceptance bandwidth depends on the temperature derivative of the birefringence and is obtained similarly to the angular bandwidth, with the result for Type I phasematching in negative uniaxial media:

$$|T - T_{\rm pm}| < 0.221\lambda/L\partial(n_e^{2\omega} \quad n_o^{\omega})/\partial T. \qquad 5.$$

For $\lambda = 1$ μm, $L = 1$ cm, and $\partial(n_{2\omega} - n_\omega) = 10^{-5}$ K^{-1}, the temperature acceptance is $|T - T_{\rm pm}| < 2.2$ K.

In general, the wavelength acceptance of an SHG crystal is much larger than the linewidth of a single frequency laser. However, for low coherence sources like some diode lasers, and for mode-locked lasers with large spectral bandwidths, the wavelength acceptance can be an important issue. Proceeding similarly as for the other bandwidths, we find for Type I interactions in negative uniaxial media

$$|\lambda - \lambda_{\rm pm}| < 0.221\lambda/L\partial(n_e^{2\omega} - n_o^{\omega})/\partial\lambda, \qquad 6.$$

with similar expressions for other phasematching schemes. Typical values for the acceptance bandwidth for SHG in the visible are on the order of 1 nm. The bandwidth decreases with increasing difference between the wavelength derivatives of the refractive indices at the fundamental and the second harmonic, and hence typically gets smaller for interactions involving wavelengths approaching the UV or IR absorption edges, where the dispersion is larger. An accidental degeneracy of these derivatives (or of the temperature derivatives in Equation 5) can lead to wavelength (temperature) noncritical phasematching, with large spectral (temperature) acceptance bandwidth. The phasematching loci available in biaxial crystals

with a low-birefringence plane can again be advantageous in the search for such noncritical operating points.

Focusing

To this point we have considered only plane wave interactions. In any real system, the interacting beams will be of finite extent, typically with a Gaussian transverse profile (Figure 1, second from top). For beams of finite cross-section, it is generally more useful to define the conversion efficiency as the ratio of the SH to the fundamental power, $\eta = P_{2\omega}/P_{\omega}$, rather than in terms of the intensity. Frequency conversion with Gaussian beams is discussed in detail in Reference (9). We give here only a very simple discussion that emphasizes the material parameters that influence the efficiency. The essential properties of the Gaussian beam for our purposes are its minimum radius, w_0, and the distance over which its radius remains essentially collimated (the confocal length) $b = 2\pi w_0^2 n/\lambda$ (10).

Consider first the case of noncritical phasematching. For near-field focusing ($L < b$), averaging over the cross-section of the beam, the conversion efficiency is the same as that given for plane waves in Equation 1 assuming an effective area of πw_0^2 for the Gaussian beam, that is, replacing the intensity I_ω with $P_\omega/\pi w_0^2$, which yields $\eta_{NF} = C^2 L^2 P_\omega/\pi w_0^2$. The increase in the efficiency predicted for small spot sizes breaks down for w_0 sufficiently small that $b < L$ because the shortened interaction length caused by the rapid diffraction becomes more significant than the increased peak intensity. In the near field approximation, the conversion efficiency for confocal focusing ($b = L$) is obtained by taking $w_0^2 = (L\lambda/2\pi n)$:

$$\eta_c = \gamma_{nc} L P_\omega, \qquad 7.$$

where $\gamma_{nc} = 2nC^2/\lambda = 16\pi^2 d_{eff}^2/\varepsilon_0 c n^2 \lambda^3$. Note that in this case the efficiency scales only linearly with L, rather than quadratically, as is the case for plane wave interactions. Numerical calculations show that the exact efficiency for confocal focusing is $0.8\eta_c$ and that the actual optimum, at $b = L/2.84$, is $1.07\eta_c$, but this tighter focusing is rarely used in practice. For a typical nonlinear coefficient of 5 pm/V, a wavelength of 1 μm, and a refractive index of 2, $\gamma_{nc} = 0.4\%/\text{W cm}$.

For critical phasematching, Poynting vector walkoff reduces the efficiency of the interaction by causing the SH beam to walkoff the fundamental after a distance $l_a = \pi^{1/2} w_0/\rho$. The optimum focusing remains close to confocal in the presence of walkoff, but the efficiency is reduced by an amount that depends on the walkoff parameter $B = \rho\sqrt{\pi n L/2\lambda}$. The optimum efficiency for $B = 1$ is approximately $0.58\eta_c$ and, for $B > 1.5$, can be well approximated $\eta_c/\sqrt{2B}$. In the latter limit the efficiency is given by

$$\eta = \gamma_{cr}\sqrt{L}P_{\omega}, \qquad 8.$$

where $\gamma_{cr} = 16\pi^{3/2}d_{eff}^2/\varepsilon_0 cn^{5/2}\lambda^{5/2}\rho$. Note that the efficiency now scales only with $\sqrt{L}$ and is inversely proportional to the walkoff angle ρ. For a material with the same properties as the example in the noncritical case, but having a walkoff angle $\rho = 2°$, the efficiency is $\gamma_{cr} = 0.04\%/\text{W cm}^{1/2}$.

Loss

Loss can affect efficiency either by limiting the effective interaction length or, in the case of absorption, by contributing a thermal load to the crystal that adversely affects its optical properties. Thermal effects are discussed in the section on high average power interactions. Given the extinction coefficients κ_ω and $\kappa_{2\omega}$, an exact expression for the efficiency of plane wave SHG can be obtained (11). The efficiency is significantly reduced compared to the lossless case when $\kappa L \geq 1$. For a crystal of the optimum length, $L_{\text{opt}} = (\kappa_\omega - \kappa_{2\omega}/2)^{-1} \ln(\kappa_{2\omega}/2\kappa_\omega)$, the efficiency is given, to a good approximation, by the lossless result (Equation 1) with an effective length $L_{eff} = \sqrt{2/e}(\kappa_\omega + \kappa_{2\omega}/2)^{-1}$. The combination of material properties entering into the efficiency in this case is $d_{eff}^2/[n^3(\kappa_\omega + \kappa_{2\omega}/2)]^2$. From this result we see that crystals with large, resonantly enhanced nonlinearities, such as many organic and semiconductor media, do not necessarily offer larger efficiencies than crystals having smaller nonlinearity but also lower loss. Note that the optimum length may be impractically large in the case of low-loss crystals, but efficiencies approaching the optimized result can be achieved in resonator devices, as discussed below.

Pulsed SHG

SHG from a pulsed fundamental differs from CW SHG in several ways. Here we continue to assume that the conversion efficiency is low. Effects due to the high peak conversion common with pulsed lasers are considered below.

For long pulses, the main difference is that the intensity of the pulse generally is not constant. In such a case, it is useful to define an efficiency that is the weighted average of the conversion over the duration of the pulse, which is hence the ratio of the SH pulse energy to the fundamental input energy. For pulses with a Gaussian envelope, the average energy conversion efficiency is $1/\sqrt{2}$ smaller than the intensity conversion efficiency at the peak of the pulse, and the SH pulse duration is $1/\sqrt{2}$ that of the fundamental.

Additional factors must be considered for short pulses. Here the envelope or group velocity v_g of a pulse is generally different from the phase velocity. Thus even if the interaction is phasematched (the phase velocities are

equal), the group velocities are mismatched, so that the fundamental and second harmonic pulses walk off each other as they propagate through the crystal. A close analogy exists between this time-domain walkoff and the space-domain walkoff already discussed (12). If this slippage becomes comparable to the pulse length, the efficiency is adversely affected, and the output SHG pulse can be longer than the input pulse. The characteristic length of crystal at which this occurs for a pulse of length τ is $L_\tau = \tau/(v_{g,\omega}^{-1} - v_{g,2\omega}^{-1})$ (13). This effect is obviously more serious as the pulse length is reduced and is also enhanced at wavelengths near the absorption edge of the material, where the dispersion is greater. For a typical case, SHG of 532 nm radiation in KDP, $v_{g,2\omega} = 1.84 \times 10^8$ m/s, $v_{g,\omega} = 1.94 \times 10^8$ m/s, $L_\tau = 3.5$ mm/ps. Note that a process with a large spectral acceptance bandwidth will also have a large L_τ, so that wavelength noncritical phase-matching is a significant advantage for SHG of short pulses. For phase-modulated pulses, group velocity dispersion can reduce the efficiency significantly for crystals much shorter than L_τ, especially at high conversion efficiencies (14).

Resonator Devices

For typical CW lasers, the single pass conversion efficiency is too low for practical applications. Resonant devices, where the nonlinear crystal is placed either in a Fabry-Perot cavity external to the pump laser (Figure 1, center) or inside the pump laser cavity (Figure 1, second from bottom), have much larger conversion efficiencies because intracavity circulating intensities are much larger than the input intensity. Because the finesse of the cavity, and hence the resonant enhancement of the intensity, are inversely proportional to the total loss, these devices require crystals with low extinction coefficients.

Consider first externally resonant SHG (15, 16). The nonlinear crystal is placed in a ring Fabry-Perot cavity resonant at the fundamental frequency with an input mirror with transmission T, an output mirror that is a high reflector for the fundamental and has 100% transmission at the SH, and fixed losses A_f exclusive of extinction in the nonlinear crystal itself. If T is chosen equal to the round-trip losses in the cavity, all the input power is coupled into the cavity, and the device is said to be impedance matched. In the limit of an undepleted pump, the circulating fundamental power in the cavity is enhanced by a factor $1/(\kappa_\omega L + A_f)$, and the output power by the square of this factor. For a noncritically phase-matched crystal and confocal focusing of the pump, the optimum length in this limit is A_f/κ_ω, in which case the efficiency is the same as that of a confocal device of length $1/4\kappa_\omega A_f$, and we find the combination of material properties entering into the efficiency in this case is $d_{eff}^2/(n^2\kappa_\omega)$. For a device

with $A_f = 0.3\%$, $\kappa_\omega = 3 \times 10^{-3}\ \mathrm{cm}^{-1}$, the optimum length is 1 cm, and the enhancement over the single pass efficiency is 3×10^4. When the conversion efficiency is large enough to deplete the pump, the analysis becomes more complicated. It can be shown (S. Schiller, personal communication) that under these conditions, the power necessary to achieve 50% conversion efficiency is

$$P_{50,nc} = 8\kappa_\omega A_f/\gamma_{nc}, \qquad 9.$$

and thus the same material figure of merit pertains as for the undepleted pump case. For $\gamma_c = 0.4\%/\mathrm{W\ cm}$, and the loss figures given above, $P_{50,nc} = 18\ \mathrm{mW}$.

For a critically phasematched interaction, the analysis is slightly different. Assuming that the walkoff parameter B is sufficiently large that Equation 8 applies for the single pass conversion efficiency, the optimum crystal length is $A_f/3\kappa_\omega$, and the efficiency for an undepleted pump is the same as that of an optimally focused device of length $0.11A_f^3\kappa_\omega$. The combination of material properties entering into the efficiency in this case is then $d_{eff}^2/(n^{5/2}\kappa_\omega^{1/2}\rho)$. Incorporating pump depletion, the power necessary for 50% conversion efficiency is

$$P_{50,cr} = 6.2(A_f^{3/2}\kappa_\omega^{1/2}/\gamma_{cr}). \qquad 10.$$

From Equations 9 and 10 it can be seen that critical phasematching increases the necessary power by a factor of $0.77\rho\sqrt{\pi n A_f/\kappa_\omega \lambda}$. For a critically phasematched device with $\rho = 2°$ and other parameters as the noncritical device above, seven times more power is required.

The importance of low loss crystals and mirrors for resonator SHG is clear from Equations 9 and 10. In many cases, monolithic cavities are used to minimize surface losses. The above analysis applies to monolithic cavities as well, but the extinction coefficient κ_ω must be replaced by $2\kappa_\omega$ to account for the entire beam path lying inside the crystal. For short pulses, synchronous pumping in which the resonant cavity length is equal to the laser cavity length can lead to high efficiencies (18).

For intracavity SHG, the crystal is placed inside the resonator of the pump laser (19, 20). In these devices, the cavity mirrors are high reflectors for the fundamental wavelength, and the output coupling is through conversion of the circulating fundamental field to SH. The crystal length providing optimum output coupling depends on the properties of both the laser and the nonlinear material. At the optimum coupling, the single pass SHG conversion for a circulating power equal to the saturation power is equal to the total linear losses in the cavity, i.e. for noncritical phasematching

$$L_{opt} = (A_l + A_f)/\gamma_{nc} P_s, \qquad 11.$$

and for critical phasematching with $B > 1.5$,

$$L_{opt} = [(A_l + A_f)/\gamma_{cr} P_s]^2, \qquad 12.$$

where A_f and A_l are the fixed losses associated with the nonlinear crystal and the laser, respectively, P_s is the saturation power, defined as the product of the saturation intensity of the laser medium and the area of the laser mode, γ_{nc} and γ_{cr} are the SH conversion coefficients defined in Equations 7 and 8, and we have assumed optimal focusing in the nonlinear crystal. A useful definition of the efficiency of the frequency conversion of such a device is the ratio of the second harmonic output power to the fundamental output power that would be obtained from the laser with optimal linear output coupling.

$$\eta = P_{2\omega}/P_{\omega,noSH} = \left[\frac{1-\sqrt{[(A_l+A_f)/g_0]}}{1-\sqrt{A_l/g_0}}\right]^2, \qquad 13.$$

where the unsaturated gain of the laser is g_0. Note that for a lossless crystal, $\eta = 1$, and the same output power can be extracted at the second harmonic as could be obtained at the fundamental without SHG. In this discussion we have neglected the extinction coefficient of the nonlinear crystal because its inclusion leads to unwieldy expressions for the optimized performance. Significant reductions in the efficiency occur when the crystal loss is comparable to the fixed loss in the system, i.e. when $\kappa_\omega/\gamma_{nc} \approx P_s$ for noncritical phasematching and when $\kappa_\omega/\gamma_{cr}^2 \approx P_s^2/(A_f + A_l)$ for critical phasematching. As a numerical example, consider a noncritically phasematched crystal with $\gamma_{nc} = 0.4\%/\text{W cm}$, in a laser cavity with a saturation power of 1 W, $g_0 = 10\%$, and $A_f = A_l = 0.25\%$. We find $L_{opt} = 1.25$ cm, and $\eta = 85\%$.

Efficient CW SHG devices have been based on both intracavity and external cavity doubling. Various considerations such as frequency locking the laser to external cavity doublers and excess amplitude noise in intracavity doublers (21, 22) often influence the practical tradeoff between these approaches.

High Peak Power SHG

High peak power SHG differs from CW SHG in two important regards: the high single-pass conversion efficiency renders the simple undepleted-pump expression given in Equation 1 no longer applicable, and surface damage effects often limit the minimum allowable spot size. Taken together, these effects dictate quite different design criteria than are used

in low peak power SHG. The exact results for plane wave SHG when η_0 is large and $\delta \neq 0$ are complicated (23). For our purposes, two important features emerge: the phase-matching curve narrows with increasing η_0, thus reducing the various acceptance bandwidths; and the efficiency is no longer a monotonically increasing function η_0, but rather shows a peak at an optimum value that depends on δ. It can be shown that the peak efficiency is a function only of the ratio η_0/δ^2.

To find the prescription for optimizing the efficiency (8, 24–26), we first recall a basic result of diffraction theory: that the angular divergence of a beam is inversely proportional to the spot size, i.e. $\Delta\theta = M\lambda/\pi nw$, where w is the radius of the beam, and M is a measure of the beam quality, equal to 1 for an ideal diffraction limited beam. Because of this angular spread, any finite size beam will be somewhat phase-mismatched, by an amount $\delta = \beta\Delta\theta L/2$ inversely proportional to the spot size, and $\beta = \partial\Delta k/\partial\theta$ can be related to the crystal parameters of Equation 3. At a fixed input power, the intensity (and hence the nonlinear drive) is inversely proportional to the beam area. Taken together with our result for the angular phase-mismatch, this means that the ratio η_0/δ^2 is independent of the length of the crystal and the spot size, and hence is a constant Φ for a given material and input beam, given by

$$\Phi = \eta_0/\delta^2 = (4\pi/M^2)P/P_{th}, \qquad 14.$$

where P is the power of the input beam, and the threshold power, a material property, is given by

$$P_{th} = (\beta\lambda/nC)^2. \qquad 15.$$

To achieve 50% conversion efficiency requires $\Phi > 2$, i.e. the laser power must exceed $M^2P_{th}/2\pi$. If less power is available, then no combination of crystal length and circular spot size will yield 50% efficiency.

In general, the maximum attainable efficiency η_m is given by

$$\eta_m = 1 + 1/(2\Phi) - \sqrt{[1 + 1/(2\Phi)]^2 - 1}, \qquad 16.$$

which is attained at an optimized nonlinear drive $\eta_{0,\text{opt}}$ given by

$$\eta_{0,\text{opt}} \approx (\pi^2/4\eta_m)\ln[1/(1-\eta_m^2)]. \qquad 17.$$

From this result and Equation 1, we then find the optimum aspect ratio $L/w = (\pi\eta_{0,\text{opt}}/C^2P)^2$. Note that using a crystal longer than this specification for a given spot size or focusing more tightly than this specification for a given crystal length will actually reduce the efficiency, even though the nonlinear drive is increased. The minimum allowable spot size is determined by the surface damage threshold, $w_{\min} = \sqrt{P/\pi I_{dam}}$, so the shortest

possible crystal (obtained for $w = w_{\min}$) compatible with both optimizing efficiency and avoiding surface damage is $L_{\min} = \sqrt{\eta_{0,\text{opt}}/C^2 I_{dam}}$.

For beams that are nonuniform in space or time, the efficiency is lower than that predicted by Equation 16. For a beam Gaussian in space and time, reasonable accuracy is obtained if the beam width and the pulse width are measured at the $1/e^2$ points.

Other effects that can reduce the efficiency in high peak power SHG are two photon absorption and the Kerr effect. The former leads to absorption losses proportional to the intensity squared, which can often be larger than the linear absorption for radiation with a photon energy greater than half the bandgap of the crystal. The latter leads to an intensity-dependent refractive index that can reduce the beam quality through self-focusing or spoil the phasematching with a radially varying effective refractive index.

High Average Power SHG

As the fundamental power in a device increases, absorption can lead to a significant temperature rise in the nonlinear crystal which, through thermo-optic effects, can spoil the phasematching of the interaction or cause deterioration of the beam quality through thermal lensing, or both. If we consider a flat-top beam with average power P_{av} and radius w passing through a cylindrical crystal of radius R, absorption coefficient α, and thermal conductivity k_{th}, whose surface is held at a fixed temperature, the temperature profile inside the beam is parabolic, with an increase from center-to-edge of the beam of $\delta T = \alpha P_{av}/4\pi k_{th}$, independent of both R and w. The temperature rise from center-to-edge of the crystal is larger by a factor $[2\ln(R/w)+1]$. In most cases, the average temperature rise can be corrected by appropriately reducing the surface temperature. The variation across the beam is more serious, since it cannot readily be corrected by simple means.

The phase mismatch associated with a temperature rise δT depends on the thermal derivatives of the refractive indices and the length of the crystal: $\delta_{th} = 2\pi[\partial(n_{2\omega} - n_\omega)/\partial T]\delta T L/\lambda$. Thus a power P_{av} passing through a crystal of length L causes a mismatch

$$\delta_{th} = [\partial(n_{2\omega} - n_\omega)/\partial T]\,(\alpha L/2\lambda k_{th})P_{av}. \qquad 18.$$

Thus once a maximum allowable thermal detuning is specified, the maximum allowable average power is determined by the combination of material properties, $[\partial(n_{2\omega} - n_\omega)\partial T]\alpha/k_{th}$. References (27, 28) discuss these effects, including beams of Gaussian profile.

In CW devices, the power is limited either by thermal dephasing or by thermal lensing. Reference (28) shows that in the low conversion limit, the efficiency at the optimized operating point falls by 50% when $\delta_{th} = 5.7$. A

useful figure to characterize the power handling capability of a material is the ratio of the conversion efficiency to the thermal dephasing. With Equation 7 for noncritical phasematching, we find for a confocally focused interaction

$$\frac{\eta_c}{\delta_{th}} = \frac{2\lambda k_{th}\gamma_{nc}}{\alpha\partial(n_{2\omega}-n_{\omega})/\partial T}. \qquad 19.$$

It is interesting to note that this ratio is independent of both the length of the crystal and the input power and, for a given length, η/δ_{th} gets monotonically worse with increasing spot size. For critical phasematching a similar expression obtains, but the ratio now gets worse with the square root of crystal length. The focal strength of the thermal lens created by a beam of radius w and power P in a medium of length L is given by (29)

$$f_{th} = \frac{2\pi k_{th}}{\alpha\,\partial n/\partial T}\frac{w^2}{LP_{av}}. \qquad 20.$$

Proper design can minimize the effects of this spherical lens (30), but aspheric terms present for non-flat beams lead to beam distortion and losses (29).

For both these effects, we have included only the thermal loading by the fundamental. If there is significant single-pass conversion efficiency, the thermal loading due to the second harmonic must be considered as well, by replacing α_ω with $\alpha_\omega+\eta\alpha_{2\omega}$. This consideration is particularly important when η is large and, as is often the case, the absorption at the second harmonic is significantly higher than that at the fundamental. In such cases, the axial variation in the temperature rise (due to the axial variation in $P_{2\omega}$) can be significant (31).

At high conversion efficiencies, the narrowing of the phase matching peak must be taken into account. One can reasonably require that the thermal detuning (Equation 18) be smaller than the angular detuning already present (Equation 14). For very high peak and avcrage powers, beam diameters larger than the crystal thickness can be preferable, especially when cooling through the face of the crystal is possible by, for example, flowing a cooling gas over the plate. Thermal management and device optimization in these extreme cases are discussed in Reference (24).

In addition to the thermooptic effects considered in this section, absorption can lead through thermal expansion to inhomogeneous stress fields that can affect phasematching and beam quality (although the birefringence of phasematchable crystals greatly reduces the thermal depolarization) and contribute to thermal lensing. In extreme cases, these stresses

can lead to thermal fracture of the crystal. Stress optic and thermal fracture effects in high power SHG are discussed in Reference (24).

Sum and Difference Frequency Generation

Detailed discussion of sum and difference frequency generation (SFG and DFG) is beyond the scope of this chapter. Discussions of these interactions can be found in References (8, 25, 32, 33). The general considerations are similar to those presented here for SHG. The plane wave conversion efficiency for SFG, defined as I_3/I_1, is obtained by multiplying Equation 1 for SHG by $(\lambda/\lambda_3)^2 I_2/I_\omega$, and that for DFG, defined as I_1/I_2 by multiplying Equation 1 for SHG by $(\lambda/\lambda_1)^2 I_3/I_\omega$. In most materials, sum frequency generation can be phasematched at wavelengths somewhat shorter than can be reached by SHG, and difference frequency generation can be phasematched at wavelengths substantially longer than the longest fundamental wavelength that phasematches for SHG. The anlysis of focused SFG and DFG is somewhat more complicated than for SHG and is discussed in References (9, 33, 34).

Resonant cavity techniques similar to those used in SHG have also been applied to SFG (35, 36).

Parametric Amplification and Oscillation

In a DFG process, where a strong pump at frequency ω_3 interacts with a weak beam at ω_2 to generate an output at ω_1, the signal at ω_2 experiences parametric gain, that is, for every photon generated at the "idler" frequency ω_1, a photon is also generated at ω_2. This phenomenon leads to exponential amplification of the signal beam. For the case of degenerate parametric amplification, where $\omega_1 = \omega_2 = \omega_3/2$, the parametric gain is numerically equal to the SHG conversion efficiency at the same input power, and hence can be on the order of 1% even for CW pumps. If such a parametric amplifier is placed in a cavity with mirrors reflective at one or both of ω_1 and ω_2 (singly and doubly resonant), coherent output at these frequencies can build up with only the pump frequency input if the gain exceeds the loss, much as in a conventional laser. The output frequency is dictated by the phasematching condition in the crystal, so that such an optical parametric oscillator (OPO) can serve as an efficient source of tunable radiation, with a tuning range limited in principle only by the phasematching range for DFG. Detailed discussion of these devices is again beyond the scope of this chapter. References (34, 37) discuss parametric amplification and oscillation in detail. Reference (38) is a current review. Here we confine the discussion to the relation of material properties to threshold power conditions.

The parametric gain at degeneracy is $g = \eta_0$, where η_0 is the nonlinear

drive given in Equation 1 which, together with the total cavity losses at the signal and idler frequencies, A_{t1} and A_{t2}, determines the CW threshold condition. For a singly resonant OPO, $g_{th} = 2A_{t2}$, so $I_{3,SRO} = 2A_{t2}/C^2L^2$. For noncritical confocal focusing, we have with Equation 7, $P_{3,SRO} = 2A_{t2}/\gamma_{nc}L$. For a doubly resonant OPO, $g_{th} = A_{t1}A_{t2}$, so $I_{3,DRO} = A_{t1}A_{t2}/C^2L^2$. For confocal focusing, $P_{3,DRO} = A_{t1}A_{t2}/\gamma_{nc}L$. With 1% losses at ω_1 and ω_2, we find for $\gamma_{nc} = 0.4\%/\text{W cm}$ and $L = 1$ cm, $P_{3,SRO} = 5$ W, and $P_{3,DRO} = 25$ mW. For a low loss device the doubly resonant OPO threshold can be two orders of magnitude smaller than that of a singly resonant OPO, but tuning and frequency stability issues become much more complex in doubly resonant OPOs. For the high pump powers involved in singly resonant OPOs, the thermal dephasing and lensing effects discussed previously must be considered.

In pulsed OPOs, the threshold condition is somewhat different if the pump pulse duration τ becomes less than the build-up time for the signal in the OPO. In such devices, it is more useful to quote a threshold pump pulse fluence (energy/area), rather than pump intensity. The threshold condition is (39)

$$E_{3,SRO} = \frac{4.5}{C^2L^2}\tau\left(\frac{15L}{\tau c} + A_{f,2} + \ln 2\right)^2,$$

where we have assumed pump and signal spot sizes are equal. As the fluence is generally limited by the surface damage threshold of the crystal, and the threshold fluence is inversely proportional to the square of the crystal length, there exists a minimum crystal length such that threshold is reached without causing surface damage. Since efficient operation generally requires pumping several times threshold, high gain and high damage thresholds are important attributes of crystals for OPO applications.

Modifications to these considerations for picosecond and femtosecond OPOs are discussed in References (38, 40).

MATERIALS PROPERTIES

Relatively very few materials find application in nonlinear optics. The physics of the frequency conversion process place severe demands on potential NLO crystals. Of roughly 20,000 crystalline phases surveyed, only a few percent offer even the combination of a non-zero nonlinear coefficient and sufficient birefringence for phasematching. Beyond the NLO physics exist the additional practical demands of mechanical and chemical stability and the possibility for production in the form of adequately-sized and adequately uniform single crystals. In actuality, only

several tens of different phases have ever been applied to practical NLO frequency conversion.

Tables 1 and 2 (at the end of the chapter) are a compilation of relevant properties and figures of merit for some of the more common NLO materials. Table 1 lists microscopic material properties, including transparency range, nonlinear susceptibilities, losses, thermo-optic coefficients, thermal conductivity, and damage threshold. Table 2 comprises parameters relevant to particular interactions, where we have chosen SHG of 1.06 and 0.532 nm radiation as representative visible and UV interactions, and SHG of 4 μm radiation as a representative mid-IR interaction. This table contains two parts, basic parameters of the interaction including phase-matching angles, effective nonlinear coefficients, angular, temperature and wavelength bandwidths, and walkoff angle, and various figures of merit that combine several of these basic properties. The figures of merit include the threshold power P_{th} (Equation 15) relevant to high peak power interactions, the power necessary to reach 50% conversion in a resonant doubler P_{50} (Equation 9 or 10 with $A_f = 1\%$), the thermal dephasing normalized to the confocal conversion efficiency (Equation 19), the thermal focusing per unit input power (Equation 20) for a confocally focused beam, and the nonlinear drive for a pump intensity equal to the damage intensity.

Several points are notable about Table 1 and Table 2 in particular and NLO material properties in general. First, accurate physical property data are difficult to obtain. Necessary measurements are often subtle and tedious. Errors are common. Although to the best of our knowledge, the data in the tables are accurate, they and other NLO literature data should be applied with caution, especially common are errors and inconsistencies concerning designation of crystallographic axes (5). The figures given for losses and damage intensities in the literature vary widely. The data in Table 1 reflect the low end of literature values for losses. Thermo-optic data are spotty, and often not sufficiently accurate for reliable calculation of acceptance bandwidths. Where available, experimental bandwidths are given in Table 2.

Second, following the earlier discussions of NLO fundamentals, the linear optical and thermal properties of a material are in general as important as its NLO coefficients. Historically, there has been an unfortunate tendency for NLO materials to be evaluated on the basis of their optical nonlinearity alone.

Third, again following the earlier discussions, different figures of merit apply to different application regimes. As is evident from a cursory examination of the tables, there exists no "all around best" NLO material. A material well-suited to one application might be a poor candidate for a different set of operating conditions.

Fourth and finally, although some NLO material properties are determined solely by the identity of the crystalline phase, many other properties are highly processing-dependent. Thus important properties can vary from one crystal to the next, and tabulated data may be useful only in providing rough guidelines.

We turn now to a brief consideration of each of the important NLO material properties.

Optical Transmission and Loss

For an NLO interaction to be viable in a given material, the material must be reasonably transmissive to the optical frequencies involved. As relevant to NLO, the identity of the crystalline phase largely determines the nominal range of transmission with the high-frequency cutoff due to interband electronic transitions and the low-frequency cutoff caused by phonon absorption.

Within a material's nominal transmission range, relatively small amounts of optical loss can be critical, particularly for NLO configurations involving high average power, where low absorption is critical, or high finesse resonators, where both absorption and scattering adversely affect performance. Such losses can be extremely processing-dependent.

Sources of extrinsic absorption include chemical impurities, color centers, inclusions, and free carriers. Extrinsic absorption effects can be highly wavelength-specific. Extrinsic scattering is caused by mechanical strain, grain boundaries, compositional inhomogeneities, or inclusions. The scattering power of sources much larger than the optical wavelength is largely wavelength independent, while that due to sources much smaller than the optical wavelength tends to vary inversely with the fourth power of the wavelength. The wavelength dependence of scattering effects from sources of intermediate size falls between these two extremes.

Surface losses often dominate volume losses within a material's nominal transmission range. Surface loss effects depend on the cutting, polishing, and coating processes performed in preparing the crystal surface, as discussed below.

Nonlinear Susceptibility

A material's nonlinear optical response is determined by the atomic arrangement in the material. For NLO coefficients to be non-zero, the point group must lack a center of inversion symmetry. References (11, 41, 42) discuss in detail the relationship between chemical bonding and nonlinear susceptibility. Tabulations of NLO coefficients for a wide range of materials can be found in References (43, 44).

As they relate a polarization response to two electric fields, a material's

NLO coefficients are elements of a third-rank tensor. The effective NLO coefficient d_{eff} obtained by projecting the polarization of the input and output fields onto the **d** tensor can be highly directionally-dependent and thus in a given material, can vary dramatically among different NLO interactions requiring different phasematching directions and polarizations. References (5, 6) outline procedures for calculating specific d_{eff} values. In general, within its transmission range, a material's NLO coefficients do not depend strongly on optical frequency, nor are they highly processing-dependent.

Birefringence and Phasematching

Although the refractive indices are largely determined by the identity of the crystalline phase, phasematching in nonlinear optics depends upon the relatively much smaller difference between refractive index values for different polarizations. Thus small refractive index variations within a crystal or from one crystal to another can result in large differences in birefringence and related phasematching characteristics. Such variations are commonly due to compositional variations or internal strain within a crystal. Optimal phasematching of some NLO interactions may require birefringence uniformity better than $\pm 10^{-6}$/cm. Such tight tolerance places stringent demands on process-dependent material quality.

The thermal and angular derivatives of the birefringence, important for phasematching bandwidths, are relatively insensitive to materials processing. As is the case for d_{eff}, however, these properties can be highly directionally-dependent and thus may vary dramatically for a given material among specific NLO interactions. Thermally induced birefringence change depends strongly on a crystal's optical absorption properties, particularly in high average power applications.

Laser Damage Resistance

Numerous undesirable effects can occur when a laser beam impinges on an NLO crystal. Catastrophic failure of the crystal can be initiated on its surfaces or in its bulk, or the beam, without destroying the crystal, can induce uncontrollable changes in the crystal's properties. A material's laser damage resistance is difficult to quantify. Damage processes tend to be highly probabilistic in nature. Moreover, damage mechanisms depend strongly on surface cleanliness and sample history as well as laser parameters such as energy, wavelength, pulse length, mode structure, spot size, and beam waist location.

In most NLO applications, catastrophic laser damage is most likely to be initiated on a crystal's surface. Catastrophic surface damage is particularly common in pulsed, high peak power applications. Although the physical mechanisms involved are complex, they tend to involve the pres-

ence on the surface of imperfections such as residual scratches, polishing-induced inclusions, and foreign particulates that serve to locally intensify the electric field. Surface damage resistance thus depends strongly on the cutting, polishing, coating, and cleaning processes performed in preparing the crystal surfaces. Because of residual stresses and adhesion non-uniformities common in deposited thin-films, optical coating typically lowers the surface damage resistance of an NLO crystal. As a rough guideline for extrapolating tabular data, the damage threshold laser fluence (energy per unit area) for a given surface scales with the square root of the pulse length and inversely with the square root of the spot size. In most cases, Fresnel reflection effects result in higher field intensity at a crystal's exit surface than at its entrance surface (45). Catastrophic surface damage is thus most commonly observed to be initiated on the exit face.

Catastrophic bulk damage generally occurs via a thermally-induced fracture mechanism. Extrinsic absorption or particulate scatter can increase a crystal's internal thermal load. Mechanical strain can lower a crystal's fracture resistance. Bulk catastrophic damage resistance thus depends strongly on processing.

In a number of NLO materials, incoming or generated optical radiation induces changes in the material's properties, most commonly the refractive indices (known as the photorefractive effect), or the optical absorption (the photochromic effect). Photorefraction involves charge migration in and around the irradiated region. Photochromic effects tend to involve single or multiphoton generation of color centers. Although such optically induced property changes are generally not in themselves catastrophic, they can adversely affect phasematching stability or output beam quality and can lead to other damage phenomena that are catastrophic. Optically-induced property changes are typically more common and more severe at high average powers. They generally depend strongly on wavelength, operating temperature of the crystal, and crystal composition, particularly the presence of key impurity species. In most cases, induced property changes are reversible; after removal of the incoming radiation, the crystal tends toward recovery of its original properties. The recovery process can usually be accelerated with higher temperatures.

MATERIALS PROCESSING

The size, availability, cost, and properties of NLO crystals are all largely determined by materials processing. Many steps are involved in producing a crystal for NLO application. Any single processing step can be critical in determining a key feature of the crystal. The science and technology of NLO materials processing are, in general, very different from the science

and technology of NLO applications. Historically, this difference has led to unfortunate misunderstandings and inefficiencies in relationships between materials producers and materials users. In this section, we consider processing of inorganic NLO crystals in light of the applications-driven materials requirements already discussed.

Crystal Growth

With rare exception, crystalline phases are required for finite optical nonlinearity. Macroscopic single crystals are required for efficient phase-matching and acceptably low optical loss. Crystal growth is thus a central element in the processing of NLO materials. References (46–48) are general overviews of the science and technology of crystal growth.

NLO applications require single crystals ranging in size from several millimeters on edge to nearly a meter across. Certain applications demand loss values below 0.1%/cm and birefringence uniformity in excess of 10^{-6}/cm. Crystal size, optical loss, and optical uniformity, as well as ultimate crystal cost, tend to be dominated by the crystal growth process.

The majority of synthetic crystals are produced by growth from the liquid phase. As discussed below, a variety of techniques are practiced, involving either solidification of a melt or controlled recovery of solute from solution. Melt solidification typically offers the advantages of efficiency and relative simplicity. Growth from solution is generally more broadly applicable. For most materials, there emerges a preferred crystal growth technique. The process-dependent properties and limitations of a crystal tend to reflect the inherent nature of that growth technique.

Common to all processes of crystal growth from a fluid phase are the microscopic growth mechanisms: transport of growth units (atoms, ions, molecules, or clusters) to the growth interface, interface attachment of growth units, removal from the interface of any solvent or rejected impurity species, and removal of the latent heat of crystallization. The overall kinetics of a given growth process are usually dominated by one of these mechanisms. Understanding and engineering a given growth process generally amounts to understanding and engineering its kinetically dominant microscopic mechanism.

Also common to all crystal growth processes is the importance of preparation of a starting chemical charge. For growth of most oxide crystals, initial charge composition control to 1 part in 10^4 is a practical goal at present. This requires attention to issues of moisture incorporation in raw chemicals, volatilization losses during heating and reaction and, possibly, isotopic ratios of critical elements. Impurity species present special problems. They can influence charge composition control, crystal growth mechanisms, and application-related properties of the grown crystal. Impurity

levels are often limited by available raw chemicals and can vary greatly from one material to another. In oxide charges, individual impurity concentrations in the parts per million level are common.

CZOCHRALSKI GROWTH The Czochralski process, diagrammed in Figure 2 (top left), is the most common technique for crystal growth from a melt. A liquid of the same or nearly the same composition as that desired for the crystal is prepared and contained in a crucible at a temperature slightly above its freezing point. An oriented seed crystal of the desired crystalline phase is lowered into contact with the melt surface. Through a combination of thermal conduction through the seed and programmed reduction of heat input to the melt, oriented solidification on the seed is initiated. By

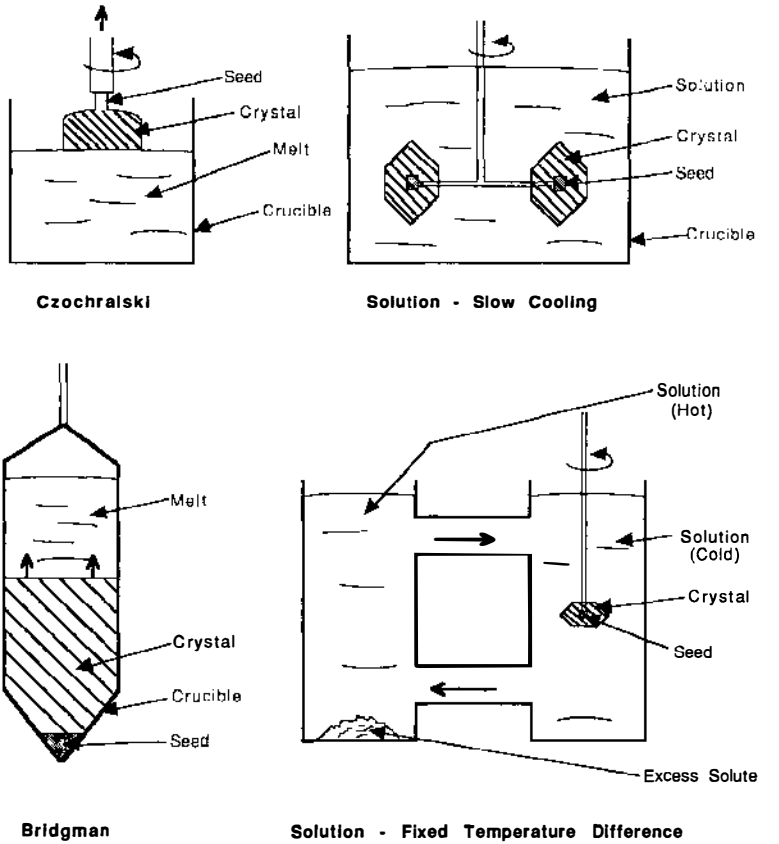

Figure 2 Crystal growth process schematics.

slowly raising the seed, a significant portion of the melt can be converted into an oriented single crystal. By controlling the rate of seed withdrawal and the heat input to the melt, the cross-section of the growing crystal can be controlled. Weight sensors or optical monitors can be applied to establish an automated closed-loop system for this purpose.

The kinetics of Czochralski growth are usually dominated by removal of the heat of crystallization. The seed/crystal and possibly the crucible are continuously rotated to encourage azimuthal symmetry of the thermal field. As a consequence, Czochralski-grown crystal boules tend to be nearly cylindrical in shape. Through the Czochralski process, crystals of a number of materials can be routinely grown with diameters over 50 mm. Typical growth rates for oxide crystals are several mm/h. Semiconductors are grown about ten times faster.

Internal strain in a Czochralski-grown crystal is due to dislocations that are either grown into the structure at the solid/liquid interface, or generated through thermal stresses on cooling. Although thermal gradients through a crystal or across its growth interface are usually responsible for these dislocations, gradients are necessary for effective diameter control. Thermal engineering in a Czochralski process is thus critical and often subtle. Various radiation reflection and gas flow baffling schemes are often employed around and above a growing crystal. The thermal field in the melt depends on fluid flow, which can be influenced through the imposed crystal and crucible rotation program.

Additional quality issues with Czochralski-grown crystals concern compositional inhomogeneity. Preferential rejection or incorporation of species at the growth interface results in a changing melt composition as growth proceeds. Such species segregation can involve impurities, dopants or, in the case of a non-elemental crystal, one of the crystal's component species. Only in the case where a liquid can be crystallized into a solid of precisely the same composition, known as congruent solidification, is there no progressive change in melt composition.

A changing melt composition can cause problems in several ways. A gradual compositional variation usually results along the crystal's growth axis. Often, convective instabilities in the melt near the interface result in periodic compositional fluctuations. These take the form of evenly-spaced striae perpendicular to the growth direction. A crystal with a spatially varying composition can have a varying thermal expansion coefficient, which adds to thermal stress problems on cooling. A large enough discrepancy between liquid and solid compositions at the interface can result in the dominance of interface attachment control of the overall growth kinetics. This can increase dislocation generation at the growth interface and possibly render the diameter control algorithm ineffective. Due to

these problems with species segregation, doping an otherwise congruent system generally adds significantly to the difficulty in growing a high-quality crystal.

For most Czochralski-growth operations, a relatively high melting point accounts for numerous practical problems. Potential crucible materials for the hot and often highly corrosive melts are limited. In growth of oxides, precious metal crucibles are typically used, although even in this case, crucible corrosion can lead to metallic inclusions in grown crystals. Mechanical and structural furnace components are restricted as well, and component degradation can easily lead to melt contamination.

Perhaps the greatest general limitation to Czochralski growth is the relative rarity of crystalline phases that are sufficiently close to melting congruently to enable application of the technique.

BRIDGMAN GROWTH In a Bridgman process, diagrammed in Figure 2 (bottom left), a melt contained in a crucible is progressively frozen from one end to the other to yield a single crystal of a shape defined by the crucible's inner surface. Growth can be initiated through spontaneous nucleation or seeded growth can be achieved from one end of the crucible by controlled limitation of the initial melting process. Progressive solidification is achieved by either translating the crucible through the furnace, translating the furnace relative to a stationary crucible, or programmed cooling of a stationary crucible and furnace.

The kinetics of Bridgman growth are generally dominated by heat removal. For optical crystals, growth rates are typically several mm/hour and final effective diameters are usually no greater than several tens of mm.

Compared to Czochralski growth, a Bridgman process is typically simpler and less costly. In some cases, volatile melts are more easily accommodated. Compositional homogeneity issues and crucible corrosion effects are similar between the two processes, as are many of the difficulties associated with high process temperatures. Relative disadvantages of a Bridgman process include lack of operator visibility, although in some cases, use of transparent crucibles and furnaces can avoid this limitation. Other disadvantages concern the relative difficulty of influencing and controlling fluid flow patterns and the resulting thermal field and heat transfer distribution. Perhaps the most significant difficulty with Bridgman growth involves deleterious mechanical interaction between crucible and crystal on cooling. Differential thermal expansion and surface adhesion commonly give rise to high degrees of internal crystal strain.

GROWTH FROM AQUEOUS SOLUTION In crystal growth from aqueous solution, a volume of water is saturated with the material to be crystallized.

The material is recovered in single crystal form by deliberately lowering its solubility in the water, commonly by lowering the solution's temperature. In practice, this can be accomplished through a number of methods, including slow cooling of a single volume of solution (Figure 2, top right), pumped flow of solution between saturation and growth chambers maintained at different temperatures (Figure 2, bottom right), and gravity-driven solution transport between saturation and growth regions established in a single chamber through imposition of a temperature gradient. For materials having a relatively small variation of aqueous solubility with temperature, growth can sometimes be driven through an evaporation process.

Except for experimental work, seed crystals are always employed, and they are in most cases entirely submerged in solution. Growth kinetics are typically dominated by the interface attachment mechanisms. Crystals are faceted, reflecting the fact that individual layers of growth units each spread out to cover a growing surface at a rate faster than that at which new layers are generated. The particular facets that appear reflect the surface energy anisotropies involved in these interface attachment mechanisms. Multiple crystals are often grown simultaneously in the same chamber. Typical linear growth rates for facets advancing in the direction of their normals are several mm/day. Crystals can be grown having linear dimensions of several hundred mm. Solution chambers can have volumetric capacities in excess of 100 liters.

A high degree of temperature uniformity and stability is necessary to avoid both dissolution/re-growth flaws and undesirable spurious nucleation of additional crystals. In practice, restricting short-term thermal fluctuations in the region of the growing crystals to less than several hundredths of one degree centigrade is a reasonable goal. With growth run durations up to tens of weeks, equipment reliability is critical, and safeguards against electrical power interruption are warranted.

The most common flawing effect in growth from aqueous solution involves uncontrolled inclusion of volumes of growth solution in growing crystals. Such inclusions must be avoided in fabricating devices. They also commonly result in deleterious internal strain in neighboring regions of unflawed material. The mechanism for inclusion flaws generally involves insufficient mass transport of growth units to certain regions of a growing interface. Lateral progression of growth layers is starved by lack of growth units at the leading edge. The resulting pileup of growth units leads to instability whereby overgrowth occurs across the top of the pileup, thus effecting an inclusion. Inclusion problems are exacerbated at high growth rates and with large crystals having corresponding large-area facets. Avoiding inclusion flawing requires understanding and control of fluid

flow patterns to ensure sufficient exposure of all growing facets to the bulk of the growth solution. A variety of crystal mounting, crystal rotation, and solution stirring approaches can be applied to address these issues.

Impurity incorporation phenomena in the growth of faceted crystals are notably different from those encountered in heat transfer-dominated melt growth. Impurity segregation effects can vary between facets that are not crystallographically equivalent. Neighboring regions of a crystal can thus have significantly different impurity concentrations. It is especially common for impurities to segregate to the edges formed by abutting facets. The two-dimensional loci formed in the grown crystal by the progression of these edges are thus often marked by high concentrations of impurities and associated strain fields. These loci, known as sector boundaries, are often avoided in cutting material for device application. To reduce fabrication waste associated with avoiding sector boundaries, a growth process can sometimes incorporate means to restrict growth to a limited number of sectors. Such growth restriction can be accomplished through, for example, mechanical blocking or chemical poisoning of selected facets.

Although in comparison to melt growth, the demands on temperature, supersaturation, and fluid flow control encountered in aqueous solution growth are generally greater, the relatively low process temperatures offer significant practical advantages. Thus elaborate stirring and seed-holding mechanisms can be employed, accurate solution monitoring schemes can be set up, and a relatively broad range of materials can be exploited in crystallizer construction. Perhaps most important is the typically high degree of operator visibility enabling direct feedback on the effect of various process conditions. Analogous to melt growth, a significant general limitation to aqueous solution growth is the relative rarity of interesting crystalline phases with sufficient aqueous solubility to enable application of the technique.

GROWTH FROM HIGH-TEMPERATURE SOLUTION Also known as flux growth, growth from high-temperature solution (HTS) is probably the most broadly applicable practical crystal growth technique. For most crystalline phases of interest, a viable high-temperature solvent can be found. Thus phases that do not melt congruently or undergo destructive phase transitions on cooling and that lack appreciable aqueous solubility are candidates for HTS growth. Reference (49) covers HTS crystal growth in detail.

Depending upon the solvent concentration, which in turn tends to establish the relative degree of interface attachment resistance in the overall growth kinetics, an HTS growth process can resemble either a Czochralski

operation or aqueous solution growth. For high solute to solvent ratios, especially if the solvent consists of one of the crystal's component species, application of a sufficiently high thermal gradient can enable a thermal transport-controlled top-seeded approach similar to Czochralski growth. Compared to a melt growth operation, diameter control schemes are significantly limited and progressive variations in melt composition restrict the ultimate crystal yield. For lower solute concentrations, interface attachment dominates, and crystals grow faceted, in most configurations, totally submerged in solution. Such an immersion-seeded HTS growth process resembles aqueous solution growth with the significant added disadvantages of high process temperatures. These include limited materials for furnace, crucible, and seed-holder construction, crucible and furnace corrosion, limited measurement and monitoring capabilities, and restricted operator visibility. In some cases, a hybrid approach can be applied where thermal gradient-controlled top-seeding is followed by faceted growth progressing into the solution volume.

For most currently practiced HTS growth processes, solution volumes are in the general range of 250 cm^3 to 10 liters with linear dimensions of grown crystals in the range of tens of mm. Growth run durations range from several days in the case of some top-seeded methods to several weeks. Depending upon the growth mechanism, flawing and impurity incorporation effects resemble those in Czochralski or aqueous solution growth. If the solvent contains species foreign to the crystal, impurity concentration levels can be relatively high.

HYDROTHERMAL GROWTH For some materials of interest, application of high pressure increases aqueous solubility to an extent enabling a slow cooling or thermal gradient gravity-driven solution growth process. Such hydrothermal growth processes tend to resemble aqueous solution growth in regard to kinetic mechanisms and defect formation. Significant practical disadvantages relative to aqueous solution growth involve high process temperatures and pressures and resulting restrictions on mechanical and structural materials, measurement and instrumentation schemes, and operator visibility.

Annealing and Vapor Processing

In the processing of many NLO crystals, growth is followed by an annealing treatment at elevated temperature, often employing a specially selected atmosphere. Such annealing and vapor processing can be used to influence a variety of application-related material properties.

In the case of crystals grown at high temperature, a post-growth anneal can sometimes help to reduce internal strain by allowing dislocation climb.

Such an anneal can often be performed in the growth furnace itself. In many instances, slow and controlled cooling to room temperature is necessary to preserve the beneficial effects of the anneal. Annealing can also be performed to allow short-scale compositional fluctuations to relax through diffusion, thereby improving optical homogeneity. Another use of high-temperature annealing is to dissolve precipitates that would otherwise act as scatter sites.

High-temperature treatment in a dry atmosphere is sometimes employed to remove hydroxyl ions in crystals. Hydroxyl ion impurities resulting from undried starting chemicals or atmospheric moisture during growth are common in many oxide crystals. The resulting hydrogen-oxygen bonds effect a sometimes undesirable optical absorption peak in the 3 μm wavelength region. Removal of the hydrogen species improves transmission in this region.

For oxides and other ionic crystals, anncaling treatmcnt in an atmosphere of controlled oxygen partial pressure is often applied to influence the oxidation state of component or unavoidable impurity species. By controlling the oxidation state, optical absorption effects due to these species can be minimized.

In some cases, grown crystals are annealed in the presence of selected chemical sources, most often in the form of prepared powders. Through mechanisms involving vapor transport and solid-state diffusion, the stoichiometry of a crystal can thereby be adjusted. Such treatments may be performed to improve a material's optical transmission, adjust its birefringence, or increase its laser damage resistance.

Annealing and vapor processing treatments can be performed on entire crystalline boules or on smaller fabricated pieces. With processes often rate-limited by solid-state diffusional transport, processing durations can exceed several weeks and reduction of specimen thickness can, in these cases, reduce process times quadratically. Although atmosphere and temperature control are sometimes critical, in comparison to crystal growth, the design and execution of annealing and vapor processing technology are usually relatively straightforward.

Ferroelectric Poling

A number of interesting NLO crystals are ferroelectric. A ferroelectric crystal has an atomic structural unit cell possessing a net electric dipole moment that can be switched through external means among more than one possible orientation. In the as-grown state, a ferroelectric crystal typically consists of a multiplicity of regions called domains, within each of which the dipole orientation is uniform. Domain topology varies widely among different materials and even among different specimens of the same

material. Characteristic as-grown domain sizes vary as well, from several microns to tens of mm.

An uncontrolled multidomain state in a ferroelectric crystal is generally unacceptable for NLO application. The net NLO response is reduced, phasematching is interrupted, and the boundaries between domains can act as scattering sites. A ferroelectric crystal is thus normally "poled" prior to use to establish a single consistent dipole orientation throughout its volume.

Most ferroelectric materials undergo a displacive ferroelectric phase transition at some temperature below their melting or decomposition point. Above this temperature, commonly referred to as a crystal's Curie temperature, the net electric dipole vanishes. A ferroelectric crystal is typically poled through application of an oriented electric field or, in some cases, mechanical stress, while being cooled through its Curie temperature. Such poling can sometimes be accomplished in the growth furnace on initial cooling, but is most commonly performed as a separate post-growth operation. Depending on the poling technique and the desired dipole orientation relative to the shape of the as-grown crystal, poling is performed on either the as-grown crystal itself, or on a smaller oriented and fabricated cell.

Care is required in designing and executing a poling operation. Experimental determination of the Curie temperature is often required. Necessary magnitudes and durations of applied electric or stress fields must be established, generally empirically. Prolonged application of a DC bias can degrade a crystal through ion migration-induced compositional variation or field-assisted indiffusion of metallic electrode species. Domain walls can resist removal through pinning effects of cracks or inclusions. Proper crystal stoichiometry and oxidation states must be preserved, as well. In some cases, annealing operations described above can be performed in conjunction with the poling process.

Orientation and Cutting

Orientation of NLO crystals is generally performed using X-ray diffraction techniques. Orientational precision in the range of 10 to 30 arc min is routinely achieved and rarely presents any limitation to NLO device performance. Reference (50) covers crystal orientation in detail.

A number of methods are used for cutting NLO crystals. Probably most common is use of an O.D. saw with a diamond-impregnated blade. Abrasive slurry can also be employed in place of the diamond. String sawing using abrasive slurry or liquid in which the crystal is soluble and wire sawing using a loop of diamond-impregnated wire are also common. Although string and wire sawing are relatively slow processes, they have

the advantage of being gentle on a crystal, thus reducing the likelihood of cracking and minimizing damage to the cut surfaces.

The primary issue in designing a cutting process for an NLO crystal is avoiding catastrophic cracking due to excessive mechanical or thermal stress. Although surface damage is important, an adequate lapping operation can generally compensate.

Grinding, Lapping, and Polishing

The basic objective in preparing surfaces on an NLO crystal is to enable optical beams to enter and exit the crystal with minimum disruption both to the beams and to the crystal. Specifically, the issues of concern are generally scattering and absorption of the optical beams and catastrophic laser damage to the crystal. A surface preparation process starts with an as-cut surface and progresses through a sequence of increasingly finer-scale material removal. Initial stages of surface preparation involve purely mechanical mechanisms of material removal. Final stages involve mechanisms that can be mechanical, chemical, or a combination of both. In progressing through the sequence, it is of paramount importance that each stage remove all the damage, including especially sub-surface damage, introduced by the previous stage. References (51, 52) review crystalline surface preparation.

With as-cut surfaces that are particularly rough or slightly misoriented, fixed abrasive grinding is performed. Grinding can be performed with a moving abrasive belt or, more commonly, a rotating turntable. Material removal rates are relatively high and care must be taken not to crack a crystal through overstressing or overheating. De-poling is a concern with ferroelectric materials.

Lapping is generally performed on a rotating turntable equipped with spindle or planetary fixturing. Abrasive slurry, water or oil-based, is continuously supplied to the surface of the lap. Alumina powder, with particle sizes specifiable over a range from roughly 5 to 30 μm, is a widely-used abrasive. For most NLO crystals, a sequence of two or three progressive lapping stages is typical.

Polishing processes are similar in their mechanical design to lapping processes. Material removal schemes vary more widely. At the extreme of mechanical removal, use of a water or oil-based suspension of submicron diamond particles is a common technique. Toward the other extreme, an aqueous suspension of colloidal silica has a caustic pH and removes material through chemical action. A single polishing stage is typical.

All crystal fabrication operations require some means to secure the crystal. Mechanical fixtures are time-consuming to fabricate and can stress crystals, possibly leading to cracking or de-poling. Mounting with waxes

and epoxies is common, although thermal stresses during wax mounting can cause problems and both waxes and epoxies can be difficult to remove from the crystal after fabrication. Cleaning is generally performed using organic solvents. Ultrasonic enhancement of a cleaning operation can be useful if the material itself is immune to any attendant ultrasonic damage.

Coating

In many NLO applications, it is desirable to maximize the fraction of the radiation that actually passes through the crystal. This is typically accomplished by applying appropriate anti-reflection coatings to the crystal's surfaces. In the case of monolithic resonator devices, high-reflection coatings are necessary. Such optical coatings function as interference films. With desirable reflection or anti-reflection properties often at a combination of discrete wavelengths, coating designs can be complicated, comprising, in some cases, more than ten individual layers. Defects and absorption in an optical coating typically result in a significant decrease in resistance to laser damage relative to the uncoated crystal. In general, optical coating design involves optimization between the better reflectance properties obtainable with complex coating designs and the higher damage resistance, durability, and processing reproducibility associated with having fewer coating layers. A variety of thin-film deposition techniques are used in depositing NLO crystal coatings. These include sputtering, electron beam deposition, and ion beam deposition.

A number of difficulties are commonly encountered in coating NLO crystals. Some NLO crystals have relatively low indices of refraction. Coating materials for these crystals are restricted to those having relatively low indices in order to preserve simplicity of the coating design. Many NLO crystals are pyroelectric, that is, their surfaces can develop a static electric charge in response to a change in temperature. This can pose severe problems for deposition techniques requiring ramping of a crystal's temperature. Some crystals have strongly anisotropic thermal expansion behavior. This too can cause problems with coating adhesion.

SURVEY OF SELECTED NLO CRYSTALS

In this section, we consider the specific properties, processing, and applications of especially important NLO crystals. The presentation is based on the application and processing fundamentals already discussed. The reader is advised to consult the noted references directly for important details omitted from this necessarily abbreviated treatment. The applications references are representative rather than comprehensive. Reference (53) contains a much more detailed collection of current information.

Lithium Niobate

Lithium niobate (often designated $LiNbO_3$ or simply LN) is among the most thoroughly studied NLO crystals. Since the 1960s, LN has been the subject material in a number of major developments in NLO technology. Today, driven to a great extent by its commercial importance as a surface acoustic wave material, single crystal LN is manufactured by the ton. A number of reviews (54–57) have been compiled of LN's properties and processing.

As shown in Table 1, LN features a transmission range from roughly 350 to 5000 nm. Over this range, residual losses are relatively low and generally consistent from crystal to crystal. Hydroxyl ion absorption near 2870 nm is common, but can be reduced through annealing. NLO coefficients are relatively high, and the birefringence is of a magnitude enabling phasematching for non-critical Type 1 SHG of a 1064 nm fundamental near 0°C.

LN can suffer from photorefractive damage when illuminated with visible radiation (54, 57). A 10 W/cm^2 beam of CW 488 nm radiation at 20°C has been observed to cause noticeable damage effects. Catastrophic surface damage thresholds are relatively low, as well. For pulsed 1064 nm lasers, 300 MW/cm^2 for 10 nsec pulses is a typical upper design limit.

The lithium niobate phase exhibits wide solid solubility ranging from 45 to over 50 mol% Li_2O (with the remainder Nb_2O_5). A congruent composition exists at roughly 48.38 mol% Li_2O (58) enabling Czochralski growth with an interface temperature near 1250°C. Boules up to 15 cm in diameter weighing over 10 kg are grown in a number of standard orientations. LN of the congruent composition undergoes a ferroelectric phase transition near 1140°C. Electric field poling is commonly performed in a post-growth operation on uncut boules. Fabrication and coating are relatively straightforward, although care is required to avoid problems caused by pyroelectric charging. Finished crystals may have dimensions in excess of 10 cm.

Because of limitations associated with photorefractive damage in the visible spectral region, notable applications of undoped, congruent-composition lithium niobate generally involve devices operating in the infrared. For over fifteen years, 1064 nm-pumped OPOs (59) and DFG of tunable infrared radiation have been in commercial use.

Doped and Off-congruent Lithium Niobate

A variety of approaches have been explored to modify lithium niobate in an attempt to circumvent limitations associated with photorefractive

damage. The growth of crystals doped with several mol% magnesium was first reported in 1980 as a means to improve LN's photorefractive resistance (60). Certain Mg-doped crystals have been measured to have a photorefractive damage threshold more than 10^5 times greater than that typical of undoped LN. Mg doping appears to have little effect on the NLO coefficients. Residual optical loss, although increased by Mg doping, is generally within a factor of 2 of that of undoped material. Birefringence generally increases with Mg concentration over the range from 0 to 5 mol%, although recent work has shown that various crystal properties, including birefringence, can be sensitive and subtle functions of Mg concentration (61). For material doped with 5 mol% Mg, non-critical Type I phasematching for 1064 nm SHG occurs near 115°C.

Mg-doped crystals are more difficult to grow with low internal strain. Although the distribution coefficient for Mg in LN is only slightly greater than unity, both striae and axial compositional variation are common features in Mg-doped crystals. The ferroelectric Curie temperature for 5 mol% Mg-doped LN is roughly 1220°C, which necessitates modification of the standard LN poling procedure. Fabrication and coating are generally similar to undoped material.

Mg-doped LN has been applied as a monolithic external cavity resonator to frequency-double 1064 nm radiation with a conversion efficiency of over 70% (62). Over 500 mW of 532 nm output were generated with no evidence of photorefractive effects. The material has also been used in a CW 532 nm-pumped doubly-resonant OPO (63). A threshold of 12 mW was reported.

Other dopants, including Zn (64) and Sc (65), have also been reported to increase photorefractive resistance in LN. A different approach to controlled modification of LN's physical properties involves preparation of crystals having Li/Nb ratios different from the congruent composition. Such crystals have been produced through modified Czochralski growth where effects of incongruency at the interface are compensated by controlled continuous addition of component species (66, 67) and through chemical vapor annealing (68), where fabricated crystals of congruent composition are heated in the presence of a relatively large lithium niobate powder source of a desired off-congruent Li/Nb ratio. There are significant processing limitations to both approaches; striae and other nonuniformities are common, particularly in the modified Czochralski-grown material, and material produced by chemical vapor annealing is restricted in size.

Most studies of off-congruent LN have involved material with Li/Nb ratios near unity. Compared to LN of congruent composition, the larger birefringence of such Li-enriched crystals requires a higher phasematching temperature for a given NLO interaction, which results in a reduced

tendency for photorefractive damage. Li-enriched LN has been reported to frequency double 1064 nm radiation at nearly 70% efficiency to produce 1.6 W of second harmonic (31). No evidence of photorefractive damage was observed at the 234°C operating temperature for noncritical phasematching.

Potassium Niobate

As presented in Table 1, potassium niobate ($KNbO_3$ or KN) is notable for its very large NLO coefficients and birefringence. The transmission range is similar to that of LN, although residual losses are generally higher and much less consistent from crystal to crystal. Evidence of relatively large nonlinear absorption has been observed (69). For 1 nsec pulses at 1064 nm, catastrophic laser damage thresholds have been measured in excess of 7 GW/cm^2 (8). Properties and applications of KN are reviewed in References (70, 71).

As KN does not melt congruently, crystals are generally grown by a top-seeded HTS growth method using several mol% excess K_2O as a solvent (72). Growth temperatures are in the vicinity of 1050°C. As-grown boules are typically several cm on edge weighing between 50 and 200 g. Two phase transitions occur between the growth temperature and room temperature. One, near 430°C, poses problems with catastrophic cracking. The second, near 200°C, is associated with ferroelectric domain orientation and re-orientation in the final room-temperature phase.

Compared to other inorganic NLO crystals, fabrication of KN is very difficult owing to the material's low Curie temperature and its pyroelectric and ferroelastic character. Mounting, cutting, polishing, and any handling in general can result in induced domain reversals. Electric-field poling is commonly performed in the temperature range between 150 and 200°C on oriented and cut cells. Poling operations are often repeated at multiple stages in the fabrication process. Problems with cracking and domain multiplicity have been observed to be exacerbated in attempts to grow and fabricate larger boules. Fabricated crystals generally have linear dimensions less than 10 mm.

Despite these significant processing limitations, KN has been the subject of notable NLO device work. KN has been temperature-tuned for noncritical SHG of fundamental wavelengths from 838 to 950 nm (73, 74). As an angle tuned, 1064 nm-pumped OPO, KN offers a low temperature-sensitivity and can produce outputs from 1380 to 4600 nm (75). KN has been applied as a temperature-tuned 532 nm-pumped OPO generating output from 880 to 1350 nm (76). More recently, externally-resonant SHG has been achieved from a 105 mW 856 nm diode laser source with efficiency near 40% (77). In other work, 48% efficient external cavity SHG of a

1.35 W 860 nm pump was achieved through careful attention to thermal lensing (78).

KTP and Homologues

Potassium titanyl phosphate ($KTiOPO_4$ or KTP) and its homologues (permutations of Rb or Cs replacing K, or As replacing P) have risen to prominence as NLO materials in the last ten years. As shown in Table 1, KTP's transmission range, NLO coefficients, and birefringence are similar to those of LN although KTP's residual absorption is notably higher. Perhaps most important for KTP are its very large thermal and angular phasematching bandwidths for SHG of fundamental wavelengths near 1064 nm. Although none of KTP's homologues have yet been studicd in as much detail, it is known that $KTiOAsO_4$ (KTA) has slightly higher NLO coefficients, but lower birefringence, which renders it unable to phasematch an SHG interaction for a 1064 nm fundamental (79).

KTP can suffer from photochromic damage when illuminated with visible or UV radiation (80). Referred to as grey-tracking, such photochromic damage is commonly observed at high NLO conversion efficiencies and high peak intensities. Photochromic damage in KTP appears to be a complex function of peak intensity, average power, wavelength, temperature, exposure duration, and processing history of the crystal. The threshold for catastrophic surface or bulk damage in KTP typically exceeds 1 GW/cm^2 for 10 nsec 1064 nm pulses. Laser damage effects in the homologues have only recently begun to be investigated. Grey-track damage has been observed in KTA (81).

Due to irreversible decomposition reactions that occur on melting, the KTP family of crystals are grown by either hydrothermal or HTS methods. Original commercial production of KTP used a hydrothermal technique (82) featuring temperatures in the range of 600°C, pressures in the vicinity of 25 kpsi, and KH_2PO_4 as a mineralizer. Such growth conditions place restrictions on furnace volume which, in turn, limit attainable crystal sizes to linear dimensions less than 1 cm on edge. Developments in hydrothermal KTP growth enabling lower temperatures and pressures (83) are expected to allow growth of larger crystals in the near future.

A number of solvents have been demonstrated for HTS growth of KTP, including potassium phosphate of a range of compositions (84, 85), potassium tungstate (86, 87), and alkali metal halides (88). The HTS growth techniques used in commercial practice generally involve immersion-seeded growth of faceted crystals. Growth temperatures range between 700 and 1000°C, depending on the solvent used. Growth runs typically last three to six weeks and yield crystals weighing up to several hundred grams with linear dimensions on the order of 50 to 100 mm. KTP

has a ferroelectric Curie temperature near 950°C. Depending on the initial growth temperature, as-grown crystal boules tend to be either single-domain or bi-domain with a single planar domain wall separating two opposed single-domain regions. A poling operation is generally not necessary. Fabrication and coating are relatively straightforward.

Processing of KTP's homologues has only been studied aggressively in the past several years, principally in the case of KTA (89). Uncontrollable domain multiplicity has been identified as a problem. Electric-field poling techniques have been of limited utility due to KTA's high electrical conductivity in the vicinity of its Curie transition between 850 and 900°C.

The large angular and temperature acceptance bandwidths and high surface damage threshold of KTP have led to its widespread use in frequency conversion applications, particularly for SHG of 1.06 μm lasers. Intracavity SHG of diode-pumped Nd:YAG with 5 mW of 532 nm output with 230 mW diode laser pump (90), and 3 W with a total of 55 W of diode laser pump power (91), has been demonstrated, the latter extracting 47% of the available IR power. Careful design is necessary in these devices to ensure stable, low noise operation. Taking advantage of the large angular acceptance of KTP, intracavity SHG of high power multi-transverse-mode lamp-pumped lasers generated 9 W of CW 532 nm radiation and 22 W average power Q-switched (92). KTP is also widely used for SHG of mode-locked lasers (91). Tunable near-infrared lasers have been shifted into the visible by sum frequency generation and into the mid-infrared by difference frequency generation (93, 94). The broad spectral bandwidths of these processes in KTP are advantageous for femtosecond pulse applications (95). Parametric oscillators, taking advantage of the high gain and damage threshold, are actively studied and have been reviewed in Reference (38). Single-frequency CW green-pumped DRO (96) and Q-switched green-pumped SRO (97) have been demonstrated, as has an efficient operation with a Q-switched 1.06 μm pump (98). A variety of picosecond and femtosecond KTP OPOs have been demonstrated, pumped with mode-locked Ti:sapphire (99) and green mode-locked Q-switched (100) and CW (101) lasers.

Borates

The borate family of NLO crystals was discovered in the early 1980s. To date, the most prominent members of the family have been the low temperature beta phase of barium metaborate (β-BaB_2O_4 or BBO) and lithium triborate (LiB_3O_5 or LBO). These materials both combine UV transparency, high damage thresholds, and adequate birefringence for phasematching a broad range of visible and UV interactions. BBO has larger nonlinear susceptibilities than LBO, and can be phasematched more

readily in the UV, but suffers from smaller angular acceptance, lower damage threshold, and is more hygroscopic. To date, there have been no reports of photorefractive or photochromic damage effects.

Although the alpha phase of barium borate melts congruently (near 1095°C), the transition to the beta phase near 925°C is accompanied by catastrophic cracking. Most BBO crystals reported to date have been grown by a top-seeded HTS growth method employing Na_2O as a solvent with growth in the vicinity of 900°C (102–105). Growth runs of four to six weeks yield lens-shaped crystal boules typically 75 mm in diameter by 20 mm in thickness at the center. Boules regularly contain spherical solvent inclusions 10 to 100 μm in diameter; oriented and fabricated crystals are usually restricted to linear dimensions less than 1 cm. An immersion-seeded HTS growth method for BBO using NaCl as a solvent has recently been reported (106). Three-week growth runs in the vicinity of 800°C yield inclusion-free fabricated specimens several cm on edge. Work has also been reported on a method for Czochralski growth of BBO from an undercooled melt; by maintaining a large axial thermal gradient, the melt crystallizes directly to form the low temperature beta phase (107, 108). Crystals up to 15 mm in diameter by 40 mm in length have been reported. Prospects for scale-up are uncertain.

BBO appears not to require ferroelectric poling. Mounting and cutting, especially of large crystals, are hampered by a tendency to crack perpendicular to the crystallographic **z**-axis. Lapping and polishing methods are restricted due to the fact that BBO is chemically attacked by water. Highly anisotropic thermal expansion can present problems in coating.

LBO has a peritectic melting point near 834°C, which precludes the possibility of preparing crystals by standard melt-growth techniques. To date, most of the LBO crystals reported have been grown by a top-seeded HTS growth method using excess B_2O_3 as a solvent. Growth temperatures range between 750 and 830°C. Growth runs of four to six weeks yield lens-shaped or cylindrical boules, depending on whether the seed is slowly withdrawn during growth. Crystals as large as 35 mm in diameter by 20 mm in length have been grown. Inclusions similar to those found in BBO grown by a top-seeded method are common. A core of spherical inclusions is typical at the center of a crystal running along its axis of growth. Surface decomposition of the upper regions of a growing crystal has been reported as a problem (109). Oriented and fabricated crystals are usually restricted to linear dimensions less than 1 cm.

LBO appears not to require ferroelectric poling. Crystals are less water-sensitive than BBO crystals. Thermal expansion characteristics complicate coating processes.

The properties and applications of BBO are reviewed in References (110,

111), and those of LBO in Reference (112). BBO can be used to generate the second through fifth harmonics of 1.06 μm radiation (111, 113) and LBO the second and third harmonics (114). For SHG of 1.06 μm, BBO has a larger temperature acceptance bandwidth, but a small angular acceptance, while LBO can be temperature-tuned for noncritical phasematching (115) and has been used to produce as much as 50 W of 532 nm radiation (116). BBO is widely used for SHG, THG, and FHG of dye (117) and Ti:sapphire (118) lasers for tunable UV radiation, and SHG of argon lasers for high power UV (119). LBO has also been successfully applied to SHG of dye (120) and Ti:sapphire lasers (118). Wavelengths as short as 189 nm have been generated by SFG in BBO (121) and 188 nm in LBO (122). OPOs pumped by the second through fourth harmonics of 1.06 μm radiation (123, 124) have been demonstrated in BBO, with tuning ranges as broad as 0.33 to 2.4 μm, and are reviewed in (38), as are synchronously pumped ps OPOs and fs parametric generation pumped with Ti:sapphire and dye lasers. Excimer and Nd:YAG harmonic pumped OPOs in LBO are reviewed in Reference (38).

KDP and Homologues

Potassium dihydrogen phosphate (KH_2PO_4 or KDP) and its homologues (including permutations of Rb, Cs, or NH_3 replacing K, or deuterium replacing H, or As replacing P) are among the most widely-used commercial NLO materials. Although members of the family have relatively low NLO coefficients, they feature, in general, good UV transmission, high birefringence, and relatively high resistance to laser damage. The deuterated homologues offer the advantage of lower residual absorption in the 1 μm wavelength range. Regarding laser resistance, the KDP family is notable for commonly displaying nearly equivalent thresholds for catastrophic bulk and surface damage; care is required in some cases to avoid focusing in the crystal's bulk.

One of the key features of KDP family crystals is their availability in large, homogeneous pieces at relatively low cost. Crystals of the KDP family are all produced through growth from aqueous solution (125). Typical growth rates are on the order of 1 mm/day. Driven by a desire for large harmonic conversion crystal plates for use in 1 μm-pumped laser fusion work, KDP crystals have been grown with linear dimensions over 50 cm. The production of such large crystals presents significant challenges to aqueous solution growth technology and has stimulated extensive research (126).

As-grown crystals are typically single domain and do not require poling. Fabrication is generally straightforward, although due to the material's aqueous solubility, oil-based abrasives are necessary. Again driven by the

need to process large crystal plates for fusion applications, significant effort has been directed toward the surface finishing and coating of KDP. Especially noteworthy are diamond-turning techniques for cutting an optical surface with no need for abrasives (127), and sol-gel coating methods responsible for substantial improvements in reliable laser damage resistance (128, 129).

The most commonly applied of these crystals is KD_2PO_4 (KD*P), which is widely used to generate the second, third, fourth, and fifth harmonics of 1.06 μm radiation (130). Very high peak and average powers, as are important for laser fusion applications, have been generated taking advantage of the low losses and large apertures available (131). SHG (132) and SFG (133) are widely used with dye lasers to extend tuning ranges into the UV. Representative of the range of properties available in other members of this family are CsD_2AsO_4 (CD*A), which noncritically phasematches for SHG of 1.06 μm radiation (134), and $(NH_3)H_2PO_4$ (ADP), which can be temperature-tuned to noncritically phasematch UV generation by SHG of wavelengths as short as 250 nm (135), and SFG of wavelengths as short as 208 nm (136). An interesting feature of this family is the possibility of spectrally wideband SHG, where the first derivative of the phasematching angle with respect to wavelength vanishes (137).

Chalcopyrites

A number of compounds sharing the chalcopyrite crystal structure find NLO application in the infrared. The most important of these to date have been silver gallium sulfide ($AgGaS_2$), silver gallium selenide ($AgGaSe_2$), and zinc germanium phosphide ($ZnGeP_2$). As shown in Table 1, these materials exhibit broad transparency far into the infrared, sufficient birefringence to enable phasematching over a major portion of the transparency range, and relatively high nonlinear coefficients. Laser damage resistance tends to be relatively low. The greatest limitation to application of the chalcopyrites has been optical loss.

Each of the three compounds mentioned melts congruently, $AgGaS_2$ at 996°C, $AgGaSe_2$ at 856°C, and $ZnGeP_2$ at 1025°C. They are in addition all reactive with oxygen and water vapor and have relatively high vapor pressures at their melting point. They are therefore all grown by the Bridgman process using sealed crucibles, typically made of silica glass (138). Growth is usually seeded to occur along the crystallographic **z**-axis in order to avoid cracking associated with polycrystallinity or, in the case of the silver compounds, anomalous **z**-axis expansion on cooling. As-grown boules range up to 4 cm in diameter by 14 cm in length. Interaction lengths in oriented and fabricated crystals are generally limited to less than 4 cm.

Crystal growth is typically followed by an annealing treatment lasting

from ten days to six weeks. In all three materials, it appears that the composition for congruent solidification is unstable at lower temperatures, which results in second-phase precipitation that severely increases optical loss. Annealing treatments in the presence of chemical powders of a composition complementary to that of the precipitating phase allow overall composition adjustment sufficient to dissolve the precipitates and reduce optical loss (139).

Chalcopyrite crystals do not require poling. Sensitivity to water generally dictates the use of oil-based abrasives for surface finishing. Some problems have been encountered with long-term surface degradation, particularly in the case of $AgGaS_2$.

This family of crystals has been applied to a broad range of IR interactions. While $AgGaS_2$ has been used for SHG of CO_2 lasers (140) and parametric oscillation (141), it has a smaller nonlinear coefficient and higher absorption at 10.6 μm than the other chalcopyrites, and so is used primarily for DFG of tunable IR radiation. In this application, the visible and NIR transparency of $AgGaS_2$ is advantageous, allowing the generation of CW (142) and picosecond pulses (143) by differencing dye or Ti:sapphire lasers, with tuning ranges as broad as 5–18 μm (144). With a larger nonlinear susceptibility, $AgGaSe_2$ has been used to efficiently double the 10.6 μm output of a CO_2 laser (145) and in a broadly tunable 2 μm-pumped OPO (146), although the latter application is limited in power scaling by residual absorption at 2 μm and the low thermal conductivity of this crystal (147). $ZnGeP_2$, with a nonlinear susceptibility twice as large as that of $AgGaSe_2$, has been used for SHG (with 80% conversion efficiency) and fourth harmonic generation of 10.6 μm radiation (148). The high thermal conductivity of $ZnGeP_2$ and improved processing to reduce optical absorption permitted operation of an efficient 2 μm-pumped OPO with pump power as large as 13 W without thermal distortions (149).

Lithium Iodate

Lithium iodate ($LiIO_3$) has been in use as an NLO material for over 20 years. As shown in Table 1, many of its application-related properties resemble those of lithium niobate. $LiIO_3$ crystals are grown from aqueous solution, although with generally more difficulty than are crystals of the KDP family. The temperature-dependence of the aqueous solubility of $LiIO_3$, in addition to being anomalous in sign, is relatively small in magnitude. Crystals are therefore grown using either multiple-zone, fixed temperature difference crystallizers, or solvent evaporation methods. Linear crystal growth rates are relatively low, typically less than 1 mm/day. As-grown boules have the shape of hexagonal cross-sectioned prisms, 50 to 75 mm in length by 25 to 50 mm across. Fabrication is generally

straightforward using oil-based abrasives. Spurious optical loss in the near-UV or near-IR can be avoided through careful attention to pH control in preparing the growth solution.

Because of its large birefringence, lithium iodate is broadly phase-matchable, but suffers from large walkoff effects that limit conversion efficiencies despite its rather large nonlinear susceptibility. Applications taking advantage of the broad tuning range are the most common. Lithium iodate has been used for tunable visible and UV generation by SHG of dye (150) and Ti:sapphire lasers (151, 152), with milliwatts of CW output up to the phasematching limit of 293 nm. Tunable MIR has been generated by DFG of dye lasers with NIR sources (153, 154), with usable output to wavelengths as long as 5.7 μm (155). Despite its wide temperature-acceptance bandwidth and low optical losses (156), lithium iodate is not widely used for SHG of 1.06 μm radiation because of the reduced efficiency caused by its large walk-off angle. As much as 700 W CW of 657 nm radiation has been generated by SHG of a 1.315 μm oxygen-iodine laser in lithium iodate (157).

NEW DIRECTIONS

Current research in inorganic NLO crystals involves all the subject areas so far presented in this review. Interesting new NLO materials are being identified and characterized. Processing technologies are undergoing advances and refinements. Perhaps most notably, work is underway involving alternative approaches to engineering the NLO interaction itself.

Exploration of New Materials

The search is ongoing for new materials with attractive application-related NLO properties. Although NLO coefficients themselves are important, exploratory work in recent years has generally focused more on linear optical properties than has historically been the case. Especially desirable are materials having birefringence appropriate to enable noncritical phase-matching of key NLO interactions.

Notable recent exploratory work has included investigation of isomorphic substitution in the KTP family of crystals (158) and further examination of borate crystals featuring UV transparency (159). Work is also underway exploring materials based on the combination of organic and inorganic components. The aim is to couple the potential for high NLO response and the structural flexibility of organics with the generally superior mechanical and thermal properties obtainable in inorganics. Recent work in this area has involved attempts to attach highly polarizable

aromatic group cations to phosphate anions by means of hydrogen bonds (160–162). Attaching smaller conjugated groups such as chiral acids to phosphate or fluoride anions is being investigated for UV applications (8).

Some of the most significant recent research in the area of new inorganic NLO crystals has involved the development of techniques to accelerate the process by which new materials are identified and characterized. Traditionally, determination of a material's fundamental NLO properties required single crystals with linear dimensions on the order of 1 cm. Significant exploratory crystal growth effort was thus necessary to determine the viability of even a single new material. A technique first reported in 1968 (163) enables approximate characterization of the SHG properties of a given material at a given wavelength utilizing a small volume of the material in powder form. Refinement of this measurement technique (164) has clarified interpretation and improved resolution. White light refractometry is a complementary technique recently developed (164) to determine approximately the phasematching properties of a similar powder sample. A double-spindle stage refractometer and nonlinear optical goniometer, capable of measuring refractive indices and nonlinear properties, respectively, of submillimeter crystallites have recently been developed and applied to surveying nonlinear materials (8, 165).

The combined use of these methods enables accurate characterization of nonlinear coefficients and phasematching properties on crystal samples of unprecedented small size, thereby accelerating the search for new NLO materials. Research programs utilizing these methods have recently been reported (8, 166). Larger crystals are still required for accurate characterization of optical loss and damage threshold although, as discussed earlier, these properties tend in any case to be especially processing-dependent.

Materials Processing Developments

Although research is currently underway into numerous aspects of the materials processing of inorganic NLO crystals, we note here only two significant trends, both involving crystal growth. First, due to its broad applicability, crystal growth from high-temperature solution is increasing in importance and related research activities are expanding as well. Historically, since relatively large single crystals were prerequisite to NLO property characterization, crystals of known interest tended to be crystals that were relatively easy to grow, often by melt growth techniques. In recent years, however, advanced NLO property characterization techniques such as mentioned above have identified interesting crystals for which no simple growth method is viable. HTS growth is often the best method available

for producing these materials with necessary dimensions. At the same time, fundamental advances have been achieved in making available control instrumentation and furnace component hardware extending the potential for applying the HTS method (103).

Second, with the general advance of crystal growth technology and increased application performance demands on NLO crystals, there is underway a gradual evolution in emphasis in NLO crystal growth research and development that may be loosely described as a shift from macro to micro issues. As effective generalized approaches are established for addressing macro problems like cracking, liquid inclusion, and spurious nucleation, micro issues such as composition and dislocation distribution, point defect equilibria, and trace impurity effects are receiving greater attention. Such a shift requires a generally more rigorous approach to the materials science of crystal growth as well as an increased reliance on sophisticated characterization techniques for compositional and structural analysis.

Extension of Existing Materials

In addition to improved processing of existing crystals, and the development of new inorganic crystals with extended phasematching ranges and/or larger nonlinear susceptibilities, research in several other types of nonlinear materials is proceeding rapidly. Two closely interrelated topics, quasi-phasematching and waveguide structures, have opened new opportunities for practical devices operating at milliwatt power levels and offer the prospect of tailoring one nonlinear medium to suit a broad range of interactions.

QUASI-PHASEMATCHING Given the paucity of crystals with appropriate combinations of linear, nonlinear, thermal, and chemical properties required for nonlinear device applications, the evident difficulty in developing reproducible growth and fabrication processes for new nonlinear crystals, and the concomitant long time scale, typically 10 to 15 years, for their widespread commercialization, it is clear that crystals with broad application ranges are very attractive. As discussed above, the requirement of adequate birefringence for phasematching, and the importance of near-noncritical phasematching, often limit the range of interactions for which a given crystal is applicable. Thus means for circumventing the limitations imposed by birefringent phasematching would have a major impact on nonlinear materials technology.

Quasi-phasematching (QPM), proposed by Bloembergen and co-workers in 1962 (167), is such a technique. In a quasi-phasematched interaction, the waves move with different phase velocities, but a periodic

structure in the nonlinear medium allows the interaction to proceed coherently through the entire length of the medium. To understand QPM, consider SHG as a prototypical interaction. Recall that in a nonphasematched interaction, the fundamental and the second harmonic waves drift in and out of phase with each other due to the phase-velocity mismatch, with a π phase shift accumulating over a distance known as the coherence length, $l_c = l/4(n_{2\omega} - n_\omega)$. The direction of the power flow depends on the relative phase of the waves, so over the first coherence length, power flows from the fundamental into the SH, while in the second coherence length, the power flows back into the fundamental. This periodic oscillation prevents significant buildup of power in the SH. In the simplest type of quasi-phasematched medium, the sign of the nonlinear susceptibility is reversed every coherence length, effectively resetting the phase difference between the nonlinear polarization and SH wave back to zero. The SH wave grows monotonically through the crystal, although at a slightly slower rate than would a perfectly phasematched interaction, with an equivalent nonlinear susceptibility of $d_{\text{QPM}} = 2d_{\text{eff}}/\pi$.

QPM has several significant advantages that offset the reduced effective nonlinearity (168). Most important, it eliminates any requirement on birefringence for phasematching. Thus any interaction involving radiation in the transparency range of the crystal is possible, and any convenient combination of polarizations can be used. In particular, all the waves can be polarized along the same axis, allowing the use of the diagonal components of the nonlinear susceptibility tensor, which are often much larger than the conventionally phasematchable components. For such interactions involving parallel polarizations, the tuning bandwidths are often large since they depend on the wavelength dispersion of the appropriate derivative of the refractive index, rather than on the difference between the derivatives for orthogonal polarizations.

The difficulty in implementing quasi-phasematched interactions is in creating the reversal of the nonlinear susceptibility every coherence length, typically several microns for visible interactions and several tens of microns for infrared interactions. Early work in QPM involved discrete plates of nonlinear crystals, each rotated 180° with respect to the previous plate, of interest primarily for infrared interactions (169, 170). More recently, ferroelectrics with periodic domain structures have been widely exploited for QPM, as sign changes in the nonlinear susceptibility are associated with the domain reversals (171–173). Crystals with periodic domain structures have been grown both by Czochralski and by pedestal growth techniques, using periodic perturbation of the growth conditions to create periodic compositional variations that in turn drive the domain reversal. Most of the work to date has involved $LiNbO_3$ (171–173) and $LiTaO_3$

Table 1[a]

		Uniaxial Crystals		
		KD*P (8, 196–200,a)	ADP (53, 194, (198–202,a,b)	CD*A (8, 134, 196, 199, 200, 203, 204)
Point group		$\bar{4}2m$	$\bar{4}2m$	$\bar{4}2m$
Refractive index	n_o	1.4931	1.5087	1.5500
	n_e	1.4582	1.4680	1.5431
Transparency (μm)		0.18–1.8	0.184–1.5	0.27–1.66
Nonlinear susceptibility[b] (pm/V)				
$d_{21} = d_{16}$		0	0	0
d_{22}		0	0	0
$d_{14} = d_{25} = d_{36}$		0.37	0.47	0.3
$d_{31} = d_{15}$		0	0	0
$d_{32} = d_{24}$		0	0	0
d_{33}		0	0	0
Thermo-optic coefficient (10^{-6} K^{-1})	dn_o/dt	−30	−52	−25
	dn_e/dt	−20	0	−16
Noncritical wavelength[c] (μm) Type I		0.519	0.524	1.045
Thermal conductivity[d] (W/m-k)	k_{11}	1.86	1.26	[1.5]
	k_{33}	2.09	0.71	—
Loss[e] (cm^{-1})	κ_o	0.012[f] $<10^{-3}$ (0.53 μm)	0.1 5×10^{-3} (0.59 μm)	0.006–0.01
	κ_e	$<10^{-3}$ $<10^{-3}$ (0.53 μm)	0.035 (0.27 μm)	
Surface damage intensity (GW/cm^2)		5 (1 ns) >8 (0.6 ns, 0.53 μm)	6 (15 ns) >8 (0.6 ns, 0.53 μm)	0.25 (12 ns)

BaB_2O_4 (8, 110, 205,a)	$LiNbO_3$ (8, 16, 57, 206–209)	$LiIO_3$ (8, 28, 156, 207, 210)	$AgGaS_2$ (212–216)	$AgGaSe_2$ (146, 213, 217–220)	$ZnGeP_2$ (53, 149, 221–224)
3 m	3 m	6 m	$\bar{4}$ 2 m	$\bar{4}$ 2 m	$\bar{4}$ 2 m
1.6551 1.5425	2.2322 2.1560	1.8567 1.7168	2.3472 2.2934	2.5912 2.5579	3.0728 3.1127
0.198–2.6	0.35–5	0.31–5 ‖c 0.34–4 ⊥c	0.5–13	0.78–18	0.74–12
−2.3 2.3 0	−2.1 2.1 0	0 0 (0)	0 0 17.5 (11.2@10.6 μm)	0 0 33 (10.6 μm)	0 0 69 (10.6 μm)
0.1 0.1 0	−4.3 −4.3 −27	4.4 4.4 4.5	0 0 0	0 0 0	0 0 0
−17 −9	5 38	−89 −75	154 (10.6 μm) 155 (10.6 μm)	70 (3.39 μm) 40 (3.39 μm)	150 170
0.409	1.062	0.378	1.8, 11.2	3.1, 12.8	3.2, 10.3[g]
0.08 0.8	[5.6] —	[1.47] —	[11.5]	[1]	[35]
[0.001–0.002]	0.0015	8×10^{-4} 2.5×10^{-3} (0.51 μm)	[0.01]	$1–40 \times 10^{-4}$ (2 μm)	[<0.01] (3–8 μm) 0.26 (2 μm)
[0.04] (0.27 μm)	0.025 (0.51 μm)	$<2 \times 10^{-4}$ 2.4×10^{-3} (0.51 μm)	[0.6] (10.6 μm)	$1.5–6 \times 10^{-2}$ (2 μm) [<0.02] (10.6 μm)	0.58 (2 μm) [0.5–0.8] (10.6 μm)
13.5 (1 ns)	10 (1 ns)	2 (1 ns)	0.025 (10 ns)	0.01–0.04 (50 ns, 2 μm)	0.05 (25 ns, 2 μm)
23 (14 ns) 32 (8 ns, 0.53 μm)	0.3 (10 ns)	1 (0.1 ns, >0.53 μm)	0.5 (10 ns, bulk)	0.02–0.03 (10 ns, 10.6 μm)	1 (2 ns, 10.6 μm)

Table 1[a] *(continued)*

		Biaxial Crystals		
		KTP (8, 93, 103, 225, 226)	$KNbO_3$ (8, 69–71, 227)	LiB_3O_5 (112, 114, 205 228, 229)
Point group		mm2	mm2	mm2
Refractive index	n_x	1.7367	2.1194	1.5649
	n_y	1.7395	2.2195	1.5907
	n_z	1.8305	2.2576	1.6052
Transparency (μm)		0.35–4.5	0.4–5.5	0.16–2.3
Nonlinear susceptibility[b] (pm/V)				
$d_{21} = d_{16}$		0	0	0
d_{22}		0	0	0
$d_{14} = d_{25} = d_{36}$		0	0	0
$d_{31} = d_{15}$		2.0	−11.3	−0.67
$d_{32} = d_{24}$		3.6	−12.8	0.85
d_{33}		8.3	−19.5	0.04
Thermo-optic coefficient (10^{-6} K^{-1})	dn_x/dt	11	60	−1.9
	dn_y/dt	13	22	−13
	dn_z/dt	16	−35	−8.3
Noncritical wavelength[c] (μm)				
Type I			0.860(a), 0.982(b)[h]	0.554(c)[i], 1.212(a)
Type II		0.990(b), 1.081(a)		1.19(b)
Thermal conductivity[d] (W/m-k)	k_{11}	2	—	[3]
	k_{22}	3	[5.6][i]	
	k_{33}	3.3	—	
Loss[e] (cm^{-1})		[3–8 × 10^{-3}]	[2–4 × 10^{-3}] (0.86 μm)	[3.5 × 10^{-4}][k]
		[0.02–0.07] (0.53 μm)	[0.05] (0.43 μm)	[3 × 10^{-3}] (0.35 μm)
Surface damage intensity (GW/cm^2)		9–20 (1 ns)	7 (1 ns)	25 (0.1 ns)
		>2 (10 ns, 0.5 μm)	>1 (10 ns)	1.4 (12 ns, 0.78 μm)

(174), which have attractive nonlinear properties and well-characterized material properties. The major difficulty in these techniques is maintaining the necessary tight control over the periodicity of the domains. Generally, the useful length of the crystal is limited to the distance over which the domain positions drift away from the nominal positions by an amount greater than the coherence length (168). Useful lengths up to about 1 mm have been demonstrated for visible light interactions (175, 176).

Practical device demonstrations of bulk QPM have been limited. SHG of pulsed CO_2 lasers in stacks of GaAs (170) and CdTe plates (169) has been successful, as has an optically contacted stack of LBO plates for SHG of 1.06 μm radiation (177), and external cavity SHG of a CW Nd:YAG laser in periodically-poled $LiNbO_3$, producing nearly 2 W of 532 nm radiation (176).

Periodic domains have also been created in planar substrates by lithographic techniques. Patterned dopant techniques, where a film on the surface of the crystal is patterned into a grating and then either indiffused into the substrate or used as a mask to control another diffusion process, have been successfully demonstrated in $LiNbO_3$ (Ti and Li diffusion) (178, 179), $LiTaO_3$ (H diffusion) (180), and KTP (Ba and Rb codiffusion) (181). Periodic electric fields, created either with a periodic electrode or with a scanned electron beam, have been applied to $LiNbO_3$ and $LiTaO_3$ (182–185). These surface domain structures have been used in conjunction with waveguide interactions, the subject of the following section.

WAVEGUIDE INTERACTIONS The efficiency of single-pass bulk frequency conversion is limited by the trade-off between tight focusing for high intensities and loose focusing for long interaction lengths (186). In a

[a] All data are for 1.06 μm and room temperature unless otherwise noted.

[b] All nonlinear susceptibilities in this table are from Reference 5 except for that of CD*A. Note that Reference 5 assumes Kleinman symmetry holds and adheres to IEEE/ANSI STD. 176-1987. The latter leads to a reversal of $d_{31} = d_{15}$ with $d_{32} = d_{24}$ relative to a widely used convention in the literature for crystals of the mm^2 class. Here we use values from Reference 5, but common literature assignment of axes.

[c] Noncritical wavelengths are given for interactions with nonvanishing d_{eff}.

[d] Square brackets enclosing the tabulated thermal conductivity indicate that the orientation dependence was not noted in the references used.

[e] Loss values are generally derived from calorimetric absorption. Scatter loss data are available for some materials, as noted in the table. Data for all distinct polarizations are not always available. Square brackets enclosing the tabulated loss indicate that the polarization was not noted in the references used.

[f] Highly deuterated (99.5%) samples have $\alpha_o = 0.001$ cm^{-1} and $\alpha_e = 0.0005$ cm^{-1} at 1.06 μm, as discussed in Ebbers, C. A., Happe, J., Nielsen, N., Velsko, S. P. 1992. *Appl. Opt.* 31: 1960–64.

[g] Note that d_{eff} vanishes for Type I phasematching at $\theta = 90°$, and there is insufficient birefringence for Type II phasematching at room temperature.

[h] Note $\lambda_{pm}(185°C) = 0.946$ (*a*) and $\lambda_{pm}(183°C) = 1.064$ (*b*).

[i] Estimated to be same as thermal conductivity of $LiNbO_3$.

[j] Note that d_{eff} vanishes for Type I phasematching for propagation along the *c*-axis.

[k] Note that these loss figures are absorption only. Reference 114 gives an extinction coefficient for LBO at 1.064 μm of 0.015 cm^{-1}.

Table 2[a]

	1.064 μm SHG					
	KD*P (24, 230, 231)	ADP (53, 230)	CD*A (134, 230, 231)		BaB_2O_4 (110, 232)	
Phasematching			$T_{pm} = 112°$			
Type	II	II	I	I	I	II
θ	54	62	82	90	23	32
ϕ	—	—	—	—	—	—
Nonlinear susceptibility[b]						
d_{eff} (pm/V)	0.35	0.39	0.30	0.30	1.9	1.6
C^2 (GW^{-1})	1.0	1.2	0.62	0.63	22	16
Angular acceptance (mrad-cm) critical (mrad-cm) noncritical	2.3	2.2	7.2	51	0.53	0.80
Walkoff angle						
ρ_ω (degrees)	1.3	1.2	0	0	0	3.8
$\rho_{2\omega}$ (degrees)	1.4	1.5	0.26	0	3.2	3.9
Temperature bandwidth (K-cm)	12	2.1	3	3.3	51	37
Wavelength bandwidth (nm-cm)	5.6	26	2.5	2.5	2	2.1
Threshold power						
P_{th} (MW)	30	27	3	NA	21	13
Resonant SHG[c]						
P_{50} (W)	120	210	46	26	3.6	5.8
Maximum drive $C^2 I_{dam}$ (cm^{-2})	5 (1 ns)	7 (15 ns)	0.15 (12 ns)	0.16	297 (1 ns)	216
Thermal dephasing[d]						
η/δ_{th}	5×10^{-4}	8×10^{-6}	5×10^{-4}	7.4×10^{-4}	0.01^{-3}	4×10^{-3}
Thermal focusing[e]						
f_{th} (cm-W)	−3.9	−0.13	−6.8		−3.8	

[a] Where available, experimental data are 1.064 SHG used rather than theoretical calculations. Thus, particular values may not be consistent with all data in Table 1. Wavelength and temperature bandwidths are especially prone to variation in the literature because they depend on small differences in large numbers.

[b] For 0.532 and 4 μm SHG, d obtained from 1.06 μm values using constant Miller's delta (CMD) scaling (Reference 5).

[c] Calculated assuming fixed losses of 1%. For critically phasematched materials for which $B_{opt} < 1.5$, Equation 10 is not valid, and P_{50} is obtained from more detailed analysis.

[d] Ratio of drive to thermal dephasing for confocally focused SHG. Ratio is independent of length for noncritically phasematched interaction. For critical phasematching, ratio is given for 1 cm long crystal. In both cases, ratio is independent of pump power.

1.064 μm SHG							
LiB_3O_5 (114, 120)		KTP (114, 233)	$KNbO_3$ (71)		5% MgO:$LiNbO_3$ (232)		$LiIO_3$ (156, 231, 232)
T_{pm} = 148°			T_{pm} = 183°		T_{pm} = 107°		
II(bc)	I(a)	II(a,b)	I(b,c)	I(b)	I	I	I
70.1	90°	90	71	90	77	90	30
90	0	23	90	90			
0.69	0.85	3.2	−11	−13	5.1	4.7	1.8
3.2	4.6	47	312	390	70	59	13
9.4	72	9	0.24	13	1.2	33	0.34
0.33	0	0.20	0	0	0	0	0
0	0	0.27	2.5	0	1.0	0	4.3
6.2	3.9	17	0.5	0.3	1.0	0.75	23
4.6	3.6	0.46		0.12	0.31	0.31	0.82
1.7	NA	0.029	4.0	NA	0.70	NA	66
17	8.6	0.28	0.24	0.01	0.38	0.05	6.6
4.5 (12 ns)	6.4	470 (1 ns)	2200 (1 ns)	2730	700	590	26 (1 ns)
0.1	0.2	0.9	0.07	0.6	0.1	0.4	0.05
−440		36	22		47		−12

[c] Focal length of thermal lens generated per watt of fundamental power in a confocally focused beam. Focal length is independent of crystal length under these conditions. Strongest component of the anisotropic lensing is given.

[f] 1.06 μm loss value, 0.002 cm^{-1} used for 0.532 μm SHG.

[g] Approximate angular average 0.25 W/m-K used.

[h] Thermo-optic data for chalcopyrites are problematic. Calculation of temperature acceptance bandwidths for $AgGaSe_2$ and $AgGaS_2$ is unreliable. Thermal focusing calculations for $ZnGeP_2$ appear to conflict with experiment (Reference 240) Absorption coefficient at 4 μm is not known, so 0.005 cm^{-1} is used for comparison purposes. 2 μm absorption is much larger than 4 μm value and is used for calculation of f_{th}.

Table 2 (*continued*)

	0.532 μm SHG				4 μm SHG		
	KD*P (199, 200,a, 234)	ADP (202,a,b, 234–237)		BaB_2O_4 (110, 111, 205a)	$AgGaS_2$[h] (214, 238)	$AgGaSe_2$[h] (239, 240)	$ZnGeP_2$[h] (7, 240)
Phase matching	$T_{pm} = 35°$	$T_{pm} = 51°$					
Type	I	I	I	I	I	I	I
θ	90	80	90	47	31	52	56
ϕ	—	—	—	—	—	—	—
Nonlinear susceptibility[b]							
d_{eff} (pm/V)	0.44	0.56	0.57	2.0	10.4	28	70
C^2 (GW^{-1})	5.9	9.3	9.6	90	14	81	292
Angular acceptance (mrad-cm) critical (mrad-cm) noncritical	16	1.4	16	0.16	3.7	6.0	5.0
Walkoff angle							
ρ_ω (degrees)	0	0	0	0	0	0	0.65
$\rho_{2\omega}$ (degrees)	0	0.62	0	4.8	1.2	0.64	0
Temperature bandwidth (K-cm)	3.0	0.44	0.54	4.0	50	50	40
Wavelength bandwidth (nm-cm)	0.13	0.13	0.13	0.073	11	22	20
Threshold power P_{th} (MW)	NA	2.1	NA	15	4.3	0.25	0.069
Resonant SHG[c] P_{50} (W)	0.24	2.7	0.72	1.3[f]	6.9	0.58	0.68
Maximum drive $C^2 I_{dam}$ (cm^{-2})	>50 (0.6 ns)	>70 (0.6 ns)		2800 (8 ns)	0.4 (10 ns)	3 (10 ns)	15 (25 ns)
Thermal dephasing[d] η/δ_{th}	0.05	0.0010	0.0013	2.5×10^{-3}	0.15	0.14	13
Thermal focusing[e] f_{th} (cm-W)	−23	−1.3	−1.3	−2.4[g]	13	1.5	1.0

waveguide, where light is confined by total internal reflection to a small region around the waveguide axis, this tradeoff is eliminated (Figure 1, bottom). The efficiency of a waveguide device is enhanced by a factor that scales as approximately L/w compared to a bulk device in the same medium, where w is a characteristic dimension of the waveguide mode. For w on the order of a few microns, and L on the order of 1 cm, the enhancement can be three orders of magnitude, thereby allowing efficient, nonresonant single-pass interactions with tens of mW of pump power.

Fabrication of a waveguide requires creation of a region of high refractive index surrounded by regions of lower refractive index (187). In oxide crystals, this is typically accomplished by indiffusion of a dopant that raises the refractive index through a lithographically defined mask that controls the lateral extent of the waveguide. In semiconductors, epitaxial growth of layers of differing composition, followed by post-growth patterning of the film is more common. Depending on the size and refractive index profile of the waveguide, and the wavelength of the radiation, one or more guided modes will be supported, each with a different modal electric field and phase velocity (modal dispersion). The mathematical description of waveguide frequency conversion is essentially identical to that of plane wave interactions, with the effective area for the waveguide interaction given by an overlap integral of the interacting modal fields (186).

As is the case in bulk media, both birefringent and quasi-phasematching are possible in waveguides. Early work in the field focused on birefringent phasematching (186), but the material requirements imposed by birefringent phasematching, compounded by the requirements of a suitable waveguide technology and adequate substrates for efficient lithography, severely limited the practicality of these devices. The advent of QPM techniques revitalized the field, as it was now possible to carry out a range of interactions in materials with established waveguide technologies, i.e. $LiNbO_3$, $LiTaO_3$, and KTP. Work has progressed rapidly in the past three years, with 10 to 20 mW of CW blue radiation generated by SHG of ≈ 100 mW IR sources in all three of these materials (183, 188, 189). IR generation by QPM DFG has also been demonstrated (190). Continued progress towards more sophisticated devices, such as integrated OPOs, is expected over the next several years.

In addition to the phasematching techniques available in bulk media, two additional techniques are available in waveguides. Modal phasematching, in which one takes advantage of modal dispersion to compensate for material dispersion, has not been widely used because of the reduced efficiency resulting from the poor overlap of the combinations of modes necessary for such interactions. The other technique, Cerenkov phase-

matching, involves generation of a SH wave that propagates out of the waveguide into the substrate at a characteristic angle such that the projection of the propagation constant onto the waveguide axis phasematches the guided fundamental radiation. Cerenkov devices suffer from a lower efficiency than all-guided mode interactions, and have an output in a characteristic half-moon pattern that is difficult to focus effectively (191, 192). The major advantages are broader tuning bandwidths, and recent results with low-angle Cerenkov devices with highly focusable output are encouraging (193). Surface-emitting SHG, the limiting case of Cerenkov SHG with counter-propagating pump beams and a Cerenkov angle of 90°, has been shown to be potentially efficient in media with extremely large nonlinear susceptibilities and high losses, such as III-V semiconductors (194, 195).

ACKNOWLEDGMENTS

We thank R. Route and R. Eckardt (Stanford University), R. Blachman and R. Norwood (Crystal Technology), G. Loiacono and R. Stolzenberger (Crystal Associates), P. Schunemann (Sanders-Lockheed), L. Shiozawa (Cleveland Crystals), W. Bosenberg (STI Optronics), S. Velsko (Lawrence Livermore National Laboratory), G. Mizell (Virgo Optics), and R. Adhav (Quantum Technology) for their gracious and valuable assistance.

Literature Cited

1. Franken, P. A., Hill, A. E., Peters, C. W., Weinreich, G. 1961. *Phys. Rev. Lett.* 7: 118
2. Care must be taken in consistent definition of fields and susceptibilities, especially given the several conventions used in the literature. A good discussion of these issues can be found in Kurtz, S. K. 1975. In *Quantum Electronics, A Treatise, Nonlinear Optics, Part A*, ed. H. Rabin, C. L. Tang, pp. 209–81
3. Yariv, A. 1989. *Quantum Electronics*, Chpt. 16. New York: Wiley Note that the convention for the nonlinear susceptibilities in this reference has d multiplied by the vaccuum permittivity
4. Yariv, A., Yeh, P. 1984. *Optical Waves in Crystals*, Chpt. 4. New York: Wiley
5. Roberts, D. A. 1992. *IEEE J. Quantum Electron.* 28: 2057–74
6. Hobden, M. V. 1967. *J. Appl. Phys.* 38: 4365–72
7. Singh, S. 1986. In *CRC Handbook of Laser Science and Technology, Volume III, Part* 1: *Nonlinear Optical Properties*, ed. M. J. Weber Boca Raton, FL: CRC Press
8. Eimerl, D., Velsko, S., Davis, L., Wang, F. 1990. *Prog. Cryst. Growth Charact.* 20: 59–113
9. Boyd, G. D., Kleinman, D. A. 1968. *J. Appl. Phys.* 39: 3597–639
10. Siegman, A. E. 1986. *Lasers*, Chpt. 17. Mill Valley CA: University Science Books
11. Chemla, D. S., Zyss, J., eds. 1987. In *Nonlinear Optical Properties of Organic Molecules and Crystals*, pp. 23–192. Orlando, FL: Academic
12. Akhmanov, S., Kovrygin, A., Sukhorukov, A., Kurtz, S. K. 1975. In *Quantum Electronics, A Treatise, Nonlinear Optics, Part B*, ed. H. Rabin, C. L. Tang, pp. 476–586. New York: Academic
13. Tomov, I. V., Fedosejevs, R., Offenberger, A. 1982. *IEEE J. Quantum Electron.* 12: 2048–56
14. Eckardt, R. C., Reintjes, J. 1984. *IEEE J. Quantum Electron.* 20: 1178–87
15. Ashkin, A., Boyd, G. D., Dziedzic, J.

M. 1966. *IEEE J. Quantum Electron.* QE-2: 109–23
16. Kozlovsky, W. J., Nabors, C. D., Byer, R. L. 1988. *IEEE J. Quantum Electron.* 24: 913–19
17. Deleted in proof
18. Persaud, M. A., Tolchard, J. M., Ferguson, A. I. 1990. *IEEE J. Quantum Electron.* 26: 1253–57
19. Smith, R. 1970. *IEEE J. Quantum Electron.* QE-6: 215–23
20. Zernike, F., Midwinter, J. 1973. *Applied Nonlinear Optics*, pp. 112–19. New York: Wiley & Sons
21. Baer, T. 1986. *J. Opt. Soc. Am. B* 3: 1175–80
22. Oka, M., Kubota, S. 1988. *Opt. Lett.* 13: 805–7
23. Armstrong, J., Bloembergen, N., Ducuing, J., Pershan, P. 1962. *Phys. Rev.* 127: 1918–39
24. Eimerl, D. 1987. *IEEE J. Quantum Electron.* QE-23: 575–92
25. Eimerl, D. 1987. *IEEE J. Quantum Electron.* QE-23: 1361–71
26. Beausoleil, R. G. 1992. *Lasers Optronics* 11: 17–21
27. Okada, M., Ieiri, S. 1971. *IEEE J. Quantum Electron.* 7: 560–63
28. Gettemy, D. J., Harker, W. C., Lindholm, G., Barnes, N. P. 1988. *IEEE J. Quantum Electron.* 24: 2231–37
29. Stein, A. 1974. *IEEE J. Quantum Electron.* 10: 427–34
30. Polzik, E. S., Kimble, H. J. 1991. *Opt. Lett.* 16: 1400–2
31. Jundt, D. H., Fejer, M. M., Byer, R. L., Norwood, R. G., Bordui, P. F. 1991. *Opt. Lett.* 16: 1856–58
32. Zernike, F., Midwinter, J. 1973. See Ref. 20, pp. 124–52
33. Warner, J. 1975. See Ref. 12, pp. 703–37
34. Byer, R. L. 1975. See Ref. 2, pp. 587–802
35. Risk, W. P., Baumert, J. C., Bjorklund, G. C., Schellenberg, F. M., Lenth, W. 1987. *Appl. Phys. Lett.* 52: 85–87
36. Kean, P. N., Dixon, G. J. 1992. *Opt. Lett.* 127–29
37. Byer, R. L. 1977. In *Nonlinear Optics*, ed. P. G. Harper, B. S. Wherrett, Chpt. 2. San Francisco: Academic
38. Tang, C. L., Bosenberg, W. R., Ukachi, T., Lane, R. J., Cheng, L. K. 1992. *Proc. IEEE* 80: 365–74
39. Brosnan, S. J., Byer, R. L. 1979. *IEEE J. Quantum Electron.* 15: 415–31
40. Cheung, E. C., Liu, J. M. 1991. *J. Opt. Soc. Am. B* 8: 1491–506
41. Chen, C. T. 1979. *Sci. Sin.* 22: 756
42. Levine, B. F. 1973. *Phys. Rev. B* 7: 2600–26
43. Singh, S. 1986. See Ref. 7, pp 3–228
44. Kurtz, S. K., Jerphagnon, J., Choy, M. M. 1979. In *Landolt-Bornstein Numerical Data and Functional Relationships in Science and Technology*, ed. K. H. Hellwege, A. M. Hellwege, pp. 671–743. Berlin: Springer-Verlag
45. Koechner, W. 1992. *Solid-State Laser Engineering* p. 572. Berlin: Springer-Verlag
46. Brice, J. C. 1986. *Crystal Growth Processes*. New York: Halsted
47. Chernov, A. A. 1984. *Modern Crystallography III—Crystal Growth*. New York: Springer-Verlag
48. Laudise, R. A. 1970. *The Growth of Single Crystals*, Englewood Cliffs, NJ: Prentice-Hall
49. Elwell, D., Scheel, H. J. 1975. *Crystal Growth from High-Temperature Solutions*. London/New York: Academic
50. Wood, E. A. 1963. *Crystal Orientation Manual*. New York: Columbia Univ. Press
51. Fynn, G. W., Powell, W. S. A. 1979. *The Cutting and Polishing of Electro-Optic Materials*. New York: Halsted
52. Bond, W. L. 1976. *Crystal Technology*. New York: Wiley
53. Dmitriev, V. G., Gurzadyan, G. G., Nikogosyan, D. N. 1991. *Handbook of Nonlinear Optic Crystals*. Berlin: Springer-Verlag
54. Rauber, A. 1978. In *Current Topics in Materials Science*, ed. E. Kaldis, pp. 481–601. Amsterdam: North-Holland
55. EMIS Datareviews Series No. 5. 1989. *Properties of Lithium Niobate*. London: INSPEC
56. Weis, R. S., Gaylord, T. K. 1985. *Appl. Phys. A* 37: 191–203
57. Prokhorov, A. M., Kuzminov, Y. S. 1990. *Physics and Chemistry of Crystalline Lithium Niobate*. Bristol: Hilger
58. Bordui, P. F., Norwood, R. G., Bird, C. D., Calvert, G. D. 1991. *J. Cryst. Growth* 113: 61–68
59. Herbst, R. L., Fleming, R. N., Byer, R. L. 1974. *Appl. Phys. Lett.* 25: 520–22
60. Zhong, G., Jan, J. Wu, Z. 1980. *Proc. 11th Intern. Quantum Electronics Conf., IEEE Cat. No. 80 CH* 1561–0. pp. 631
61. Bordui, P. F., Bird, C. D., Blachman, R., Schlecht, R. G., Zanelli, C. I. 1991. *Proc. Sagamore Army Mater. Res. Conf.* pp. 103–12
62. Gerstenberger, D. C., Olson, T. E., Tye, G. E., Wallace, R. W. 1992. In *Compact Blue-Green Lasers Technical Digest*, 6: 97–99. Washington: Opt. Soc. Am.
63. Nabors, C. D., Eckardt, R. C., Kozlov-

sky, W. J., Byer, R. L. 1989. *Opt. Lett.* 14: 1134–36
64. Volk, T. R., Pryalkin, V. I., Rubinina, N. M. 1990. *Opt. Lett.* 15: 996–98
65. Yamamoto, J. K., Kitamura, K., Iyi, N., Kimura, S., Furukawa, Y., Sato, M. 1992. *Appl. Phys. Lett.* 61: 2156–58
66. Kitamura, K., Yamamoto, J. K., Iyi, S., Kimura, S., Hayashi, T. 1992. *Int. Conf. Crystal Growth, 10th, San Diego.* p. 38 (Abstr.)
67. Furukawa, Y., Sato, M., Kitamura, K., Nitanda, F., Ito, K. 1992. *Int. Conf. Crystal Growth, 10th, San Diego.* p. 37 (Abstr.)
68. Bordui, P. F., Norwood, R. G., Jundt, D. H., Fejer, M. M. 1992. *J. Appl. Phys.* 71: 875–79
69. Polzik, E. S., Kimble, H. J. 1992. *Top. Meet. Compact Blue-Green Lasers, Santa Fe.* pp. 50–51 (Abstr.)
70. Zysset, B., Biaggio, I., Gunter, P. 1992. *J. Opt. Soc. Am. B* 9: 380–86
71. Biaggio, I., Kerkoc, P., Wu, L. S., Gunter, P. 1992. *J. Opt. Soc. Am. B* 9: 507–17
72. Shen, D. Z. 1990. *Prog. Cryst. Growth Charact.* 20: 161–74
73. Gunter, P. 1979. *Appl. Phys. Lett.* 34: 650–52
74. Baumert, J. C., Gunter, P., Melchior, H. 1983. *Opt. Comm.* 48: 215–20
75. Guyer, D. R., Bosenberg, W. R., Braun, F. D. 1991. *Proc. SPIE* 1409: 14–17
76. Kato, K. 1982. *IEEE J. Quantum Electron.* QE-18: 451–52
77. Kozlovsky, W. J., Lenth, W., Latta, E. E., Moser, A., Bona, G. L. 1990. *Appl. Phys. Lett.* 56: 2291–92
78. Polzik, E. S., Kimble, H. J. 1991. *Opt. Lett.* 16: 1400–2
79. Morris, P. A. 1992. *Int. Conf. Crystal Growth, 10th, San Diego.* p. 9 (Abstr.)
80. Tyminski, J. K. 1991. *J. Appl. Phys.* 70: 5570–76
81. Loiacono, G. M., Loiacono, D. N., McGee, T., Babb, M. 1992. *J. Appl. Phys.* 72: 2705–12
82. Gashurov, G., Belt, R. F. 1985. In *Tunable Solid State Lasers for Remote Sensing*, ed. R. L. Byer, E. K. Gustafson, R. Trebino, pp. 119–20. Berlin: Springer
83. Laudise, R. A., Cava, R. J., Caporaso, A. J. 1986. *J. Cryst. Growth* 74: 275–80
84. Gier, T. E. 1980. *US Patent No.* 4,231,838
85. Bordui, P. F., Jacco, J. C., Loiacono, G. M., Stolzenberger, R. A., Zola, J. J. 1987. *J. Cryst. Growth* 84: 403–8
86. Bellman, A. A., Brown, H., Olson, D. H., Rice, C. E. 1986. *J. Cryst. Growth* 75: 390–94
87. Cheng, G. C., Qian, Z. Q., Tang, G. K., Song, W. B., Tang, H. G. 1991. *J. Cryst. Growth* 112: 294–97
88. Marnier, G. 1988. *US Patent No.* 4,746,396
89. Cheng, L. K., Bierlein, J. D., Ballman, A. A. 1991. *J. Cryst. Growth* 110: 697–703
90. Masuda, H., Maeda, F., Oka, M., Kaneda, Y., Sugiura, M., Kubota, K. 1992. *Top. Meet. Compact Blue-Green Lasers, Santa Fe.* Pap. FA3–1
91. Marshall, L. R., Hays, A. D., Kaz, A., Burnham, R. 1992. *IEEE J. Quantum Electron.* 28: 1158–63
92. Perkins, P. E., Fahlen, T. S. 1987. *J. Opt. Soc. Am. B* 4: 1066–71
93. Baumert, J. C., Schellenberg, F. M., Lenth, W., Risk, W. P., Bjorklund, G. C. 1987. *Appl. Phys. Lett.* 51: 2192–94
94. Vanherzeele, H. 1989. *Opt. Lett.* 14: 728–30
95. Benicewicz, P. K., McGraw, D. 1990. *Opt. Lett.* 15: 165–67
96. Lee, D., Wong, N. C. 1992. *Opt. Lett.* 17: 13–15
97. Bosenberg, W. R., Guyer, D. R. 1992. *Appl. Phys. Lett.* 61: 387–89
98. Marshall, L. R., Kasinski, J., Burnham, R. 1991. *Opt. Lett.* 16: 681–83
99. Pelouch, W. S., Powers, P. E., Tang, C. L. 1992. *Opt. Lett.* 17: 1070–72
100. Ebrahimzadeh, M., Hall, G. J., Ferguson, A. I. 1991. *Opt. Lett.* 16: 1744–46
101. McCarthy, M. J., Hanna, D. C. 1992. *Opt. Lett.* 17: 402–4
102. Jiang, A., Cheng, F., Lin, Q., Cheng, Z., Zheng, Y. 1986. *J. Cryst. Growth* 79: 963–69
103. Cheng, L. K., Bosenberg, W. R., Tang, C. L. 1990. *Prog. Cryst. Growth Charact.* 20: 9–57
104. Feigelson, R. S., Raymakers, R. J., Route, R. K. 1990. *Prog. Cryst. Growth Charact.* 20: 115–60
105. Bosenberg, W. R., Lane, R. J., Tang, C. L. 1991. *J. Cryst. Growth* 108: 394–98
106. Bordui, P. F. 1992. *Top. Meet. Compact Blue-Green Lasers, Santa Fe.* p. 36 (Abstr.)
107. Itoh, K., Marumo, F., Kuwano, Y. 1990. *J. Cryst. Growth* 106: 728–31
108. Kouta, H., Kuwano, Y., Ito, K., Marumo, F. 1991. *J. Cryst. Growth* 114: 676–82
109. Bruck, E., Raymakers, R. J., Route, R. K., Feigelson R. S. 1992. *Int. Conf. Crystal Growth, 10th, San Diego*
110. Eimerl, D., Davis, L., Velsko, S., Graham, E. K., Zalkin, A. 1987. *J. Appl. Phys.* 62: 1968–83

111. Nikogosyan, D. N. 1991. *Appl. Phys. A* 52: 359–68
112. Chen, C., Wu, Y., Jiang, A., Wu, B., You, G., et al. 1989. *J. Opt. Soc. Am. B* 6: 616–21
113. Borsutzky, A., Brunger, R., Huang, C. H., Wallenstein, R. 1991. *Appl. Phys. B* 52: 53–62
114. Velsko, S. P., Webb, M., Davis, L., Huang, C. 1991. *IEEE J. Quantum Electron.* 27: 2182–92
115. Ukachi, T., Lane, R. J., Bosenberg, W. R., Tang, C. L. 1992. *J. Opt. Soc. Am. B* 9: 1128–33
116. Chernoch, J. P., Kukla, M. J., Lotshaw, W. T., Unternahrer, J. R. 1992. *OSA Proc. Adv. Solid State Lasers* 13: 386–88
117. Edelstein, D. C., Wachman, E. S., Cheng, L. K., Bosenberg, W. R., Tang, C. L. 1988. *Appl. Phys. Lett.* 52: 2211–13
118. Nebel, A., Beigang, R. 1991. *Opt. Lett.* 16: 1729–31
119. Taira, Y. 1992. *Jpn. J. Appl. Phys.* 31: L682–84
120. Kato, K. 1990. *IEEE J. Quantum Electron.* 26: 1173–75
121. Muckenheim, W., Lokai, P., Burghardt, B., Besting, B. 1988. *Appl. Phys. B* 45: 259–61
122. Borsutzky, A., Brunger, R., Wallenstein, R. 1991. *Appl. Phys. B* 52: 380–84
123. Fan, Y. X., Eckardt, R. C., Byer, R. L., Nolting, J., Wallenstein, R. 1988. *Appl. Phys. Lett.* 53: 2014–16
124. Bosenberg, W. R., Cheng, L. K., Tang, C. L. 1989. *Appl. Phys. Lett.* 54: 13–15
125. Loiacono, G. M. 1975. *Acta Electron.* 18: 241–51
126. Bordui, P. F. 1987. *J. Cryst. Growth* 85: 199–205
127. Kozlowski, M. R., Thomas, I., Edwards, G., Stanion, K., Fuchs, B., Latanich, L. 1991. *Proc. SPIE* 1561: 59–69
128. Thomas, I. M. 1991. *Proc. SPIE* 1561: 70–82
129. Thomas, I. M. 1986. *Appl. Opt.* 25: 1481–84
130. Craxton, R. S., Jacobs, S. D., Rizzo, J. E., Boni, R. 1981. *IEEE J. Quantum Electron.* 17: 1782–86
131. Linford, G. J., Johnson, B. C., Hildum, J. S., Marting, W. E., Snyder, K., et al 1982. *Appl. Opt.* 21: 3633–43
132. Ferguson, A. I., Dunn, M. H., Maitland, A. 1976. *Opt. Commun.* 19: 10–13
133. Blit, S., Weaver, E. G., Dunning, F. B., Tittel, F. K. 1977. *Opt. Lett.* 1: 58–60
134. Kato, K. 1974. *IEEE J. Quantum Electron.* 10: 616–18
135. Webster, C. R., Woste, L., Zare, R. N. 1980. *Opt. Commun.* 35: 435–40
136. Massey, G. A., Johnson, J. C. 1976. *IEEE J. Quantum Electron.* 12: 721–27
137. Webb, M. S., Eimerl, D., Velsko, S. 1992. *J. Opt. Soc. Am.* 9: 1118–27
138. Feigelson, R. S., Route, R. K. 1987. *Opt. Eng.* 26: 113–19
139. Feigelson, R. S., Route, R. K. 1990. *Mater. Res. Bull.* 25: 1503–11
140. Badvikov, V. V., Pivovarov, O. N., Skokov, Y. V., Skrebneva, O. V., Trotsenko, N. K. 1975. *Sov. J. Quantum Electron.* 5: 350–51
141. Fan, Y. X., Eckardt, R. C., Byer, R. L., Route, R. K., Feigelson, R. S. 1984. *Appl. Phys. Lett.* 45: 313–15
142. Canarelli, P., Benko, Z., Curl, R., Tittel, F. K. 1992. *J. Opt. Soc. Am. B* 9: 197–202
143. Yodh, A. G., Tom, H. W. K., Aumiller, G. D., Miranda, R. S. 1991. *J. Opt. Soc. Am. B* 8: 1663–67
144. Seymour, R. J., Zernike, F. 1976. *Appl. Phys. Lett.* 29: 705–7
145. Eckardt, R. C., Fan, Y. X., Byer, R. L., Route, R. K., Feigelson, R. S., van der Laan, J. 1985. *Appl. Phys. Lett.* 47: 786–88
146. Eckardt, R. C., Fan, Y. X., Byer, R. L., Marquardt, C. L., Storm, M. E., Esterowitz, L. 1986. *Appl. Phys. Lett.* 49: 608–10
147. Marquardt, C. L., Cooper, D. G., Budni, P. A., Knights, M. G., Schepler, K. L., et al. 1992. *OSA Annu. Meet.* Pap. TuWW5
148. Andreev, Y. M., Baranov, V. Y., Voevodin, V. G., Geiko, P. P., Gribenyukov, A. I. 1987. *Sov. J. Quantum Electron.* 17: 1435–36
149. Budni, P. A., Schunemann, P. G., Knights, M. G., Pollak, T. M., Chicklis, E. P. 1992. *OSA Proc. Adv. Solid State Lasers*, ed. L. L. Chase, A. A. Pinto. pp. 380–83
150. Welford, D., Sibbett, W., Taylor, J. R. 1980. *Opt. Commun.* 35: 283–86
151. Curley, P. F., Ferguson, A. I. 1991. *Opt. Lett.* 16: 321–23
152. Nebel, A., Beigang, R. 1991. *Opt. Lett.* 16: 1729–31
153. Bartoshevich, S. G., Mikhnyuk, I. V., Skripko, G. A., Tarazevich, I. G. 1991. *IEEE J. Quantum Electron.* 27: 2234–37
154. Heilweil, E. J. 1989. *Opt. Lett.* 14: 551–53
155. Kato, K. 1985. *IEEE J. Quantum Electron.* 21: 119–20
156. Webb, M. S., Velsko, S. P. 1990. *IEEE J. Quantum Electron.* 26: 1394–98

157. Hager, G. D., Hanes, S. A., Dreger, M. A. 1992. *IEEE J. Quantum Electron.* 28: 2573–76
158. Stucky, G. D. 1989. *Chem. Mater.* 1: 492–509
159. Chen, C., Wu, Y., Li, R. 1990. *J. Cryst. Growth* 99: 790–98
160. Masse, R., Zyss, J. 1991. *Mol. Eng.* 1: 141
161. Aakeroy, C. B., Hitchcock, P. B., Moyle, B. D., Seddon, K. R. 1989. *J. Chem. Soc. Chem. Commun.* 23: 1856
162. Kotler, Z., Hierle, R., Josse, D., Zyss, J., Masse, R. 1992. *J. Opt. Soc. Am. B* 9: 534–47
163. Kurtz, S., Perry, T. T. 1968. *J. Appl. Phys.* 39: 3798–813
164. Davis, L. Eimerl, D., Velsko, S. 1987. *Lawrence Livermore Natl. Lab.* UCRL-96109
165. Davis, L. 1987. *Lawrence Livermore Natl. Lab.* UCRL-96102
166. Velsko, S. P. 1991. In *Materials for Nonlinear Optics: Chemical Perspectives, ACS Symposium Series No.* 455, ed. S. Marder, J. Sohn, G. Stucky, pp. 343–59. Washington DC: Am. Chem. Soc.
167. Armstrong, J. A., Bloembergen, N., Ducuing, J., Pershan, P. S. 1962. *Phys. Rev.* 127: 1918
168. Fejer, M. M., Magel, G. A., Jundt, D. H., Byer, R. L. 1992. *IEEE J. Quantum. Electron.* 28: 2631–54
169. Piltch, M., Cantrell, C., Sze, R. 1976. *J. Appl. Phys.* 47: 3514–17
170. Szilagyi, A., Hordvik, A., Schlossberg, H. J. 1976. *Appl. Phys.* 47: 2025–32
171. Feisst, A., Koidl, P. 1985. *Appl. Phys. Lett.* 47: 1125–27
172. Xue, Y., Ming, N., Zhu, J., Feng, D. 1984. *Chin. Phys.* 4: 554–64
173. Magel, G. A., Fejer, M. M., Byer, R. L. 1990. *Appl. Phys. Lett.* 56: 108–10
174. Wang, W., Zhou, Q., Geng, Z., Feng, D. 1986. *J. Cryst. Growth* 79: 706–9
175. Lu, Y., Mao, L., Cheng, S., Ming, N., Lu, Y. 1991. *Appl. Phys. Lett.* 59: 516–18
176. Jundt, D. H., Magel, G. A., Fejer, M. M., Byer, R. L. 1991. *Appl. Phys. Lett.* 59: 2657–59
177. Mao, H., Fu, F., Wu, B., Chen, C. 1992. *Opt. Lett.* 61: 1148–50
178. Lim, E. J., Fejer, M. M., Byer, R. L. 1989. *Electron. Lett.* 25: 174–75
179. Webjorn, J., Laurell, F., Arviddson, G. 1989. *IEEE Photon. Tech. Lett.* 1: 316–18
180. Mizuuchi, M., Yamamoto, K., Taniuchi, T. 1991. *Appl. Phys. Lett.* 58: 2732–34
181. van der Poel, C., Bierlein, J., Brown, J., Colak, S. 1990. *Appl. Phys. Lett.* 57: 2074–76
182. Ito, H., Takyu, C., Inaba, H. 1991. *Electron. Lett.* 27: 1221–22
183. Yamada, M., Nada, N., Watanabe, K. 1992. *Integrated Photonics Research, New Orleans.* pp. 144–45 (Abstr.)
184. Kurimura, S., Miura, M., Sawaki, I. 1992. *Conf. Lasers and Electrooptics, Anaheim.* Postdeadline suppl. pp. 9–10
185. Fujimura, M., Kintaka, K., Suhara, T., Nishihara, H. 1992. *Electron. Lett.* 28: 1868–69
186. Stegeman, G. I., Seaton, C. T. 1985. *J. Appl. Phys.* 58: R57–78
187. Nishihara, H., Haruna, M., Suhara, T. 1989. *Optical Integrated Circuits*, pp. 7–43. New York: McGraw-Hill
188. Bierlein, J. D. 1991. *Integrated Photonics Research Conf. Monterey.* p. 95 (Abstr.)
189. Mizuuchi, K., Yamamoto, K. 1992. *J. Appl. Phys.* 72: 5061–69
190. Lim, E. J., Bortz, M. L., Fejer, M. M. 1991. *Appl. Phys. Lett.* 59: 2207–9
191. Taniuchi, T., Yamamoto, K. 1987. *Optoelectron. Devices Tech.* 2: 53–58
192. Jongerius, M. J., Drenten, R. R., Droste, R. B. J. 1992. *Philips J. Res.* 46: 135–266
193. Tamada, H. 1990. *IEEE J. Quantum Electron.* 26: 1821–26
194. Normandin, R., Letourneau, S., Chatenoud, F., Williams, R. L. 1991. *IEEE J. Quantum Electron.* 27: 125–27
195. Vakhshoori, D. 1991. *J. Appl. Phys.* 70: 5205–10
196. Kirby, K. W., deShazer, L. 1987. *J. Opt. Soc. Am.* 4: 1072–78
197. Smith, W. L. 1977. *Appl. Opt.* 16: 1798
198. Cleveland Crystals. 1984. Information Sheet: *Electro-optic Properties of KH_2PO_4 and Isomorphs.* Cleveland, OH
199. Barnes, N. P., Gettemy, D. J., Adhav, R. S. 1982. *J. Opt. Soc. Am.* 72: 895–98
200. Eimerl, D. 1987. *Ferroelectrics* 72: 95–139
200a. Linford, G. J., Johnson, B. C., Hildum, J. S., Martin. W. E., Snyder, K., et al. 1982. *Appl. Opt.* 21: 3633–43
201. Reintjes, J., Eckardt, R. C. 1977. *Appl. Phys. Lett.* 30: 91–93
202. Glass, A. J., Guenther, A. H. 1973. *Appl. Opt.* 12: 637–49
202a. Ferguson, A. I., Dunn, M. H., Maitland, A. 1976. *Opt. Commun.* 19: 10–13
202b. Reintjes, J., Eckardt, R. C. 1977. *Appl. Phys. Lett.* 30: 91–93
203. Quantum Technology, Inc. 1991. *Data Sheet* 707. Lake Mary, FL

204. Rabson, T. A., Ruiz, H. J., Shah, P. L., Tittel, F. K. 1972. *Appl. Phys. Lett.* 20: 282–84
205. Cleveland Crystals. 1991. Information Sheet: *Beta Barium Borate and Lithium Borate.* Cleveland, OH
205a. Nakatani, H., Bosenberg, W. R., Cheng, L. K., Tang, C. L. 1988. *Appl. Phys. Lett.* 53: 2587–89
206. Edwards, G. J., Lawrence, M. 1983. *Optic. Quantum Electron.* 16: 373–75
207. Ballard, S. S., Browder, S. J. 1986. Section 1.1.1.3. In *Handbook of Laser Science and Technology*, ed. M. J. Weber. Boca Raton: CRC Press
208. See, Y. C., Guha, S., Falk, J. 1980. *Appl. Opt.* 19: 1415–18
209. Crystal Technology, Inc. 1992. Data Sheet: *$LiNbO_3$ Lithium Niobate.* Palo Alto, CA
210. Cleveland Crystals. 1985. Information Sheet: *Lithium Iodate.* Cleveland, OH
211. Van Stryland, E. W., Williams, W. E., Soileau, M. J., Smirl, A. L. 1984. *IEEE J. Quantum Electron.* 20: 434–39
212. Boyd, G. D., Kasper, H., McFee, J. H. 1971. *IEEE J. Quantum Electron.* 7: 563–73
213. Bhar, G. C., Smith, R. C. 1972. *Phys. Status Solidi A* 13: 157–68
214. Bhar, G. C., Ghosh, D. K., Ghosh, P. S., Schmitt, D. 1983. *Appl. Opt.* 22: 2492–94
215. k_{th} for $AgGaS_2$ calculated from Wasim, S. M. 1979. *Phys. Status Solidi A* 51: K35–40 in Cleveland Crystals 1990. Information Sheet: *Silver Gallium Selenide and Silver Gallium Sulfide.* Cleveland, OH
216. Cleveland Crystals. 1990. Information Sheet: *Silver Gallium Selenide and Silver Gallium Sulfide.* Cleveland, OH
217. Boyd, G. D., Kasper, H. M., McFee, J. H., Storz, F. G. 1972. *IEEE J. Quantum Electron.* 8: 900–8
218. Barnes, N. P., Gettemy, D. J., Hietanen, J. R., Iannini, R. A. 1989. *Appl. Opt.* 28: 5162–68
219. See Reference 147, unreferenced work by Cleveland Crystals quoted for thermal conductivity of $AgGaSe_2$
220. Ziegler, B. C., Schepler, K. L. 1991. *Appl. Opt.* 30: 5077–80
221. Kildal, H., Mikkelsen, J. C. 1973. *Opt. Commun.* 9: 315–18
222. Boyd, L. D., Buechler, E., Storz, F. G. 1971. *Appl. Phys. Lett.* 18: 301–4
223. Bhar, G. C., Ghosh, G. C. 1980. *IEEE J. Quantum Electron.* 16: 838–43
224. Deleted in proof
225. Bierlein, J. D., Vanherzeele, H. 1989. *J. Opt. Soc. Am. B* 6: 622–33
226. Crystal Technology, Inc. 1992. Data Sheet: *KTP Potassium Titanyl Phosphate.* Palo Alto, CA
227. Crystal Technology, Inc. 1991. Data Sheet: *$KNbO_3$ Potassium Niobate.* Palo Alto, CA
228. Skripko, G. A., Bartoshevich, S. G., Mikhnyuk, I. V., Tarazevich, I. G. 1991. *Opt. Lett.* 16: 1726–28
229. Deleted in proof
230. Eimerl, D. 1987. *Ferroelectrics* 72: 95–139
231. Liu, Y. S. 1977. *Appl. Phys. Lett.* 31: 187–89
232. Eckardt, R. C., Masuda, H., Fan, Y. X., Byer, R. L. 1990. *IEEE J. Quantum Electron.* 26: 922–33
233. KTP for Second Harmonic Generation with Q-switched 1 μm Lasers. 1991. In *Crystal Technology Application Note.* Palo Alto, CA
234. Gosh, G. C., Bhar, G. C. 1982. *IEEE J. Quantum. Electron.* 18: 142–44
235. Kato, K. 1975. *Opt. Commun.* 13: 361–62
236. Zernike, F. 1964. *J. Opt. Soc. Am.* 54: 1215–20
237. Zernike, F. 1965. *J. Opt. Soc. Am.* 55: 210–11
238. Fan, Y. X., Eckardt, R. C., Byer, R. L. 1984. *Appl. Phys. Lett.* 45: 313–15
239. Kildal, H., Mikkelson, J. C. 1973. *Opt. Commun.* 9: 315–18
240. Catella, G. C., Burlage, D. S. 1993. *Advanced Solid State Lasers Topical Meeting, New Orleans.* PD3-1, PD3-3

Annual Review of Materials Science
Volume 23, 1993

CONTENTS

† Keynote Topic: Optical Materials